
Determining the Spectroscopic Quadrupole Moment Q_s of the 2_1^+ state in ^{40}Ar



**UNIVERSITY of the
WESTERN CAPE**

Makabata Jeremia
MOKGOLOBOTHO

UNIVERSITY of the
WESTERN CAPE

A thesis submitted in partial fulfillment of the requirements for the degree of
Magister Scientiae in the Department of Physics, University of the Western
Cape

March 15, 2017

Abstract

The first reorientation-effect Coulomb-excitation experiment has been performed at iThemba LABS by bombarding ^{40}Ar beams on a heavy ^{208}Pb target at a “safe” energy of $E_{lab} = 143.2$ MeV. The goal was to determine, the spectroscopic quadrupole moment, Q_s , of the first excitation 2_1^+ at 1.461 MeV in ^{40}Ar at “safe” energies. The scattered particles were detected at backward angles using a double-sided CD-type S3 silicon detector, composed of 24 rings and 32 sectors for angular distribution and Doppler correction, respectively, in coincidence with de-excited γ rays collected by 8 clover detectors in the AFRODITE array. The collected coincidence data were analysed using a state-of-the-art sorting code specially developed for this kind of measurements, which allowed, by setting up different energy and time conditions, a clean γ -ray spectrum for further analysis with the Coulomb-excitation coupled-channels code, GOSIA. A diagonal matrix element of $\langle 2_1^+ | |\hat{E}2| | 2_1^+ \rangle = +0.047(22)$ eb has been determined, which yields $Q_s(2_1^+) = +0.036(17)$ eb, after detailed GOSIA analysis and minimisation. This value is 8.5 times more precise than the only previous measurement of $Q_s(2_1^+) = +0.01(4)$ eb by Nakai and collaborators in 1970, and further supports the zig-zag of quadrupole shapes observed at the end of the sd shell. A possible explanation regards the influence of proton holes driving the nuclear shape towards an oblate configuration.

Acknowledgements

No man wakes up one day with an MSc without work being put to it, because it is so, many heavenly given beautiful souls are directly or indirectly responsible for the completion of this work. I would like to say a big thank you to the following people.

First and foremost, I would like to thank my Good friend and supervisor, Prof Nico Orce. Working with you has really been a wonderful and eventful experience I will always cherish. Your guidance and trust will forever remain trademark.

To the UWC COULEX group, Dr Mukhi Raju Kumar, Craig Venon Mehl, Elijah Hornam Akakpo, Kenzo Abrahams, Lihlele Dineo Mavela and George O'Neill. It has been a marvel working with you guys. Your inputs and ideas put bright spots on one's dark patches.

All the iThemba LABS staff and students, the very people responsible for the foundation of this work. May your great value never go unnoticed.

The MaNus/MatSci class of 2014, working with you guys has propelled me to greater heights, you shall remain part of my good memories.

Let me express my sincere gratitude to Kgashane Leroy Malatji, Phumzile Zandile Mabika, Bernadette Ribeiro, Puleng Evans Moloto and my exceptional friend, Penny Mathumba. Your support and words of encouragements have helped me through the toughest times. I shall forever be indebted to you.

I would also like to appreciate the National Research Foundation for their much needed support throughout this work.

And finally, a very big thank you to my family, kera lena bakwe ba moroka wa meetse a pula. Kere a sediba meetse kea nwele, meetse a gotswa mothopong wa bakwena. Thobela.

Table of Contents

Contents

1	Introduction	7
1.1	Scientific motivation	7
2	Coulomb Excitation	10
2.1	Rutherford Scattering	11
2.2	Basic Considerations	13
2.3	Semi-Classical Approximation	14
2.4	First-Order Perturbation Treatment	16
2.5	Second-Order Perturbation Treatment	19
2.6	Coulomb excitation analysis: GOSIA	21
3	Experimental Facility and Setup	25
3.1	iThemba LABS Cyclotron Accelerator Facilities	25
3.1.1	The AFRODITE Array	26
3.2	Detector Systems	27
3.2.1	High purity germanium (HPGe) clover Detectors	28
3.2.2	Addback	29
3.2.3	Compton Suppression	30
3.2.4	Double-Sided S3 Silicon Detector	31
3.3	Data Acquisition System and Electronics	33
3.4	The Coulomb Excitation Experiment	34
4	Data Analysis and Results	39
4.1	Interaction of Ions with Matter	39
4.2	Detectors Energy and Efficiency Calibration	40
4.2.1	Calibration of AFRODITE HPGe Clover Detectors	41
4.2.2	Gamma Efficiency Calibration	42
4.2.3	Particle Spectra Calibration	43
4.3	Background Reduction Methods	43
4.3.1	Particle- γ Coincidence Data	45
4.3.2	Energy Sharing and Inelastic Condition	46

4.3.3 Doppler Correction	48
5 GOSIA Results and Discussion	51
5.1 GOSIA Results	51
5.1.1 Minimisation and Error Estimations	51
5.2 Validation of the Obtained Matrix Elements and Discussion . . .	53
5.2.1 Discussion	54
6 Summary and Conclusions	57
A GOSIA Input files	58
A.1 OP,GDET	58
A.2 OP,THEO	59
A.3 OP,CORR,MAP,MINI and ERRO	62



List of Figures

1	sd shell Q_s values	8
2	Hyperbolic trajectory	12
3	First-order Coulomb excitation	17
4	Reorientation effect	20
5	SSC facility	26
6	AFRODITE array	27
7	Clover detector	28
8	HPGe detector's crystals	29
9	S3 detector	31
10	DDAS	34
11	Power supply	35
12	preamplifier	35
13	Safe distance	36
14	S3 setup	37
15	Interaction of projectile with target of thickness t	40
16	Gamma ray spectra of ^{152}Eu source	41
17	^{152}Eu efficiency curve	42
18	Rings particle spectra	44
19	sectors particle spectra	44
20	The time difference $\Delta t = 160$ ns for S3 coincidence window. . . .	46
21	2D particle spectra	47
22	γ -ray spectrum with no Doppler correction	48
23	Conversion of Cartesian system to spherical polar coordinate system	49
24	Doppler shift corrected spectrum	49

List of Tables

1	S3 geometry	32
2	AFRODITE geometry	35
3	Experimental details	36
4	Energy loss	38
5	Well-known ^{40}Ar $B(E2)$ values	52
6	Set of $E2$ matrix elements	52
7	Comparing previous and current measurement	55



Chapter 1

1 Introduction

The primary aim of fundamental nuclear-structure physics is to study and understand how nucleons interact with each other through the short-range and charge-independent strong nuclear force and how this interaction influences the properties of the nucleus. The development of stable and radioactive-ion-beam facilities has allowed nuclear physicists to study nuclear structure by different experimental means, where nuclei are excited to various states by colliding a projectile (energetic nucleus) with a stationary target. One of the most effective ways of probing collective nuclear properties is through the long-range Coulomb-excitation reaction.

1.1 Scientific motivation

The Coulomb-excitation process in combination with highly-efficient detector systems present a great tool to studying quadrupole collectivity in nuclei and probing nuclear-structure properties. This process employs the well-known Coulomb interaction and selectively excites collective nuclear states which decay back to the ground state through γ -ray transitions. Coulomb-excitation measurements have been carried out by various groups [1] to extract the spectroscopic (or static) quadrupole moments, or $Q_s(2_1^+)$ values, of even-even nuclei in the sd shell. Results from these measurements have been summarised by Spear's 1981 evaluation [1] and are shown in Fig. 1. The trend of measured $Q_s(2_1^+)$ values in the sd shell begins with a nearly-spherical shape in ^{18}O , rapidly changing to large prolate deformations ($Q_s(2_1^+) < 0$) before drastically flipping to a large oblate ($Q_s(2_1^+) > 0$) deformation in ^{28}Si . From this point onwards, the quadrupole shapes oscillate in a zig-zag pattern between oblate and prolate at the upper part of the sd shell before a small $Q_s(2_1^+)$ is observed near the end of the shell.

The zig-zag pattern at the end of the sd shell is more complicated than the simple picture drawn by Rowe [2] by means of the competition between the aligned coupling scheme, which tends to align the nucleon orbitals and induces

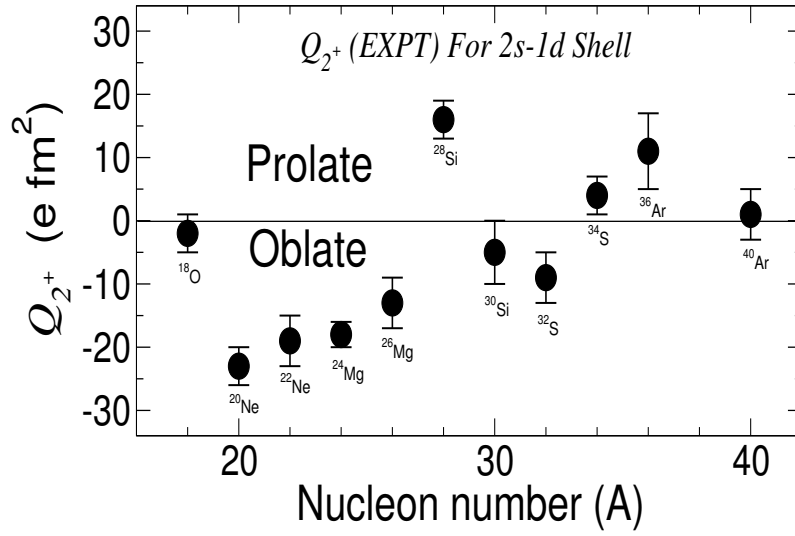


Figure 1: The $Q_2^+(2_1^+)$ values in the sd shell obtained from reorientation-effect measurements [1].

deformation, and the pair coupling scheme, which tends to scatter nucleons isotropically and drives the nucleus to a spherical shape. Rowe argues that pair coupling will dominate near the beginning of the shell, where spherical shapes are expected (as for ¹⁸O). Moving away from a magic number, particles align their orbits to form prolate shapes (rugby ball), which are enhanced in the middle of the shell. This is not really the case as ²⁰Ne surprisingly has the largest quadrupole shape within the sd shell. Near the middle of the shell, a flip-over is expected from a prolate to an oblate (or lentil-shaped) deformation, i.e., now the holes align their orbits along the polar axis, as it happens with ²⁸Si. Nuclei finally start restoring, due to the pairing of holes, spherical shapes towards the end of the shell. The zig-zag of shapes at the end of the sd shell opens stimulating questions about the physical origin of this trend and, as explained below, the reliability of the $Q_2^+(2_1^+)$ values at the end of the sd shell.

Various reorientation-effect Coulomb-excitation (RECE) measurements have recently been carried out by the University of the Western Cape group for a systematic study throughout nuclei in the sd shell. This dissertation reports on our new measurement on the $Q_2^+(2_1^+)$ value in ⁴⁰Ar using the RECE method. The only RECE measurement in ⁴⁰Ar was carried out by Nakai *et al.* in 1970

at the Berkeley Hilac using ^{40}Ar beams at unknown maximum beam energies (E_{max}) on ^{120}Sn , ^{130}Te and ^{206}Pb targets [1, 3]. Scattered particles and γ rays were detected in coincidence using particle counters at scattering angles $\theta_{lab} = 90^\circ$ and $\theta_{lab} = 160^\circ$, and one NaI counter (7.5 cm \times 7.5 cm), respectively. At that time, very little information was known about the ^{206}Pb target used in these measurements, in particular its $Q_s(2_1^+)$ value, leading them to assume that $Q_s(2_1^+)(^{206}\text{Pb}) = (0.0 \pm 0.5) |Q^{rot}|$ in their data analysis. However, this was later proven to be inaccurate as it is known that $Q_s(2_1^+)(^{206}\text{Pb}) = (0.17 \pm 0.31)|Q^{rot}|$ [1, 4]. The lack of information on E_{max} and previously unsafe RECE measurements by the same authors [1] rise the question about the validity of the measured $Q_s(2_1^+) = +0.01(4)$ eb. Surprisingly, this single measurement of $Q_s(2_1^+)$ in ^{40}Ar , with 400% uncertainty, remains the adopted value in the National Nuclear Data Center (NNDC) [5]. Although the general picture observed in the sd -shell is unlikely to undergo drastic changes, Spear [1] pointed out that additional measurements of $Q_s(2_1^+)$ are clearly required for ^{40}Ar and other nuclei.

The “safe” Coulomb-excitation particle- γ coincidence measurement for the $^{208}\text{Pb}(^{40}\text{Ar}, ^{40}\text{Ar}^*)^{208}\text{Pb}^*$ reaction has been carried out at iThemba LABS using a high efficiency experimental setup at a “safe” energy of $E_{lab} = 143.2$ MeV, calculated prior to the experimental measurement to guarantee that nuclear excitations are negligible. A heavy target enhances the reorientation effect. The de-excitation γ -rays from the excited nuclei were collected with 8 clover detectors, five at 90° and 3 at 135° , in the AFRODITE array and the scattered particle where collected with a double-sided S3 CD-type silicon detector placed at backward angles, covering a scattering angular range of $[106^\circ, 131.2^\circ]$.

The detailed experimental procedure for the current work is discussed in chapter 3, followed by data analysis in chapter 4 and discussion of the results in chapter 5. In the next chapter, the theoretical aspect of Coulomb excitation, the perturbation theory and the RECE are discussed.

Chapter 2

2 Coulomb Excitation

The Coulomb-excitation technique provides a powerful means for detailed studies of nuclear collectivity. Coulomb-excitation reactions (or Coulex) selectively populate collective states, including the first excitations of light nuclei and even low-lying collective bands in medium- and heavy-mass nuclei with cross-sections that are a direct measure of electromagnetic matrix elements. The accurate determination of both $B(E2)$ values and quadrupole moments considers the overlap of wavefunctions and are, hence, stringent tests for different nuclear models. In particular, the spectroscopic quadrupole moment of an excited state, $Q_s(J^\pi)$, is directly related to the diagonal matrix element and provides a measure of the nuclear charge distribution in the laboratory frame.

The best experimental probe to obtain information on $Q_s(J^\pi)$ with $J \neq 0, \frac{1}{2}$ requires the interaction of the nucleus with an electric-field gradient (EFG). The electric field can be generated by bombarding a target nucleus with an energetic charged projectile moving in a classical hyperbolic orbit. The objective of bombarding these nuclei is to induce an electric-field gradient at nuclear site which interacts with the nuclear quadrupole moment at some interaction energy E_Q (product of the electric-field gradient and quadrupole moment). This process induces a time-dependent interaction which gives rise to the population of excited states from the ground state. If the distance separating the two nuclei is large enough to avoid nuclear interactions, the excitation process is solely due to the well-known electromagnetic interaction between the target and the projectile [6, 7]. One of the most important aspects of this technique is the different population of magnetic substates depending on the quadrupole shape of the state. This is referred as the “reorientation effect”. Such a difference in the population of magnetic substates depending on whether the state is oblate, prolate or spherical provides a means to determine Q_s by measuring the cross section or integrated γ -ray yields as a function of scattering angle [6–8]. The sensitivity between different Q_s values is larger at backward angles [9].

The experimental measurements of Q_s values for 2_1^+ states in the sd shell nuclei are shown in Fig. 1 [1]. In the early implementation of the Coulomb-excitation technique, the de-excited γ rays were detected with NaI detectors which have large detection volume and efficiency. Advances in detector technology have seen the emergence of the much superior semiconductor-based detector such as high-purity germanium (HPGe). These detectors offer a much better resolution, and if segmented, a more enhanced Doppler capability correction compared to NaI detectors, though their detector volume is more limited.

In this chapter, the main features of the RECE technique will be briefly discussed. For an extensive study of this method, the reader should refer to Ref. [6–8].

2.1 Rutherford Scattering

When a projectile of mass M_1 , charge $+Z_1e$ and velocity v interacts with a stationary target nucleus of mass M_2 and charge $+Z_2e$, they both experience a long-range charge-dependent repulsive Coulomb force given by,

$$\vec{F} = \frac{1}{4\pi\epsilon_0} \frac{Z_1 Z_2 e^2}{r^2} \frac{\vec{r}}{r}. \quad (1)$$

The potential energy associated with the force is given by,

$$V = \frac{1}{4\pi\epsilon_0} \frac{Z_1 Z_2 e^2}{r} \frac{|\vec{r}|}{r}, \quad (2)$$

where r is the radial distance separating the two nuclei. The repulsive force causes the projectile to follow a hyperbolic trajectory such as shown in Fig. 2. If the reaction potential in equation 2 is smaller than the potential barrier, the interaction results in either elastic (Rutherford) or inelastic (Coulomb-excitation) scattering.

For Rutherford scattering, both the target and the projectile remain in their ground state after collision; hence, no γ -ray emission is associated with the elastic peaks in particle spectra. Whereas in Coulomb excitation the collision could result in the excitation of both the target and projectile. In Fig. 2 the

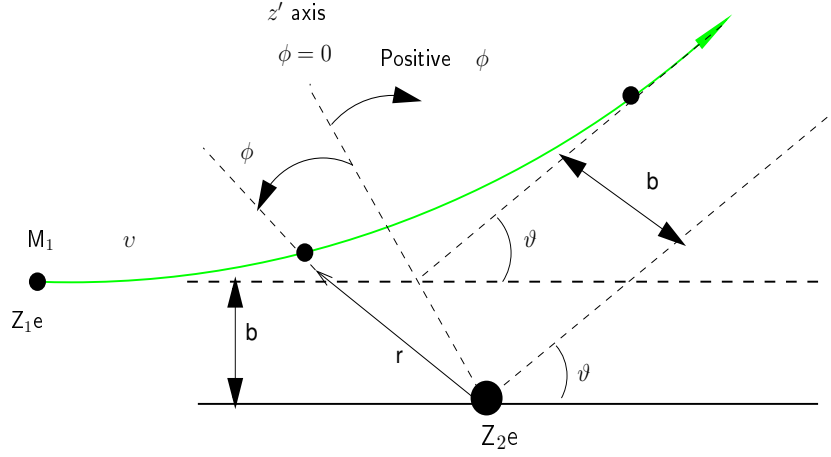


Figure 2: Schematic of the projectile's motion along the Coulomb field of the target.

impact parameter and the scattering angle (in the center of mass frame) are represented by b and ϑ , respectively. The linear momentum associated with an elastic collision changes only in direction and not in magnitude. If the mass of the target, M_2 , is much greater than the mass of the projectile, M_1 , the magnitude of both the initial and final momenta of the projectile far from the target are equal, Mv , and the target nucleus is assumed to remain stationary after the collision. The change in momentum during collision,

$$\Delta \vec{p} = 2Mv \sin \frac{\vartheta}{2}, \quad (3)$$

is equal to the net impulse due to the component of \vec{F} in the same direction and can be deduced as,

$$\Delta p = \int dp = \int \vec{F} dt = \frac{Z_1 Z_2 e^2}{4\pi\epsilon} \int \frac{\cos\phi}{r^2} dt, \quad (4)$$

where $t = (0, \infty)$ and $\phi = (-\frac{1}{2}(\pi - \vartheta), \frac{1}{2}(\pi - \vartheta))$ and v is the initial velocity of the projectile in the laboratory frame. By substituting the solution to equation 4 into equation 3, we obtain,

$$b = \frac{a}{2} \cot \frac{\vartheta}{2}. \quad (5)$$

In the study of Coulomb excitation, the parameters b , ϑ and the Rutherford cross-section, $\frac{d\sigma_R}{d\Omega}$, are of great importance since they can be varied to establish a hyperbolic trajectory of the projectile's motion. The parameter a , defined as

half the distance of closest approach in a head-on collision can be determined by equating the kinetic and potential energies in the center of mass frame,

$$E_{cm} = V_{cm} = \frac{1}{2}\mu v^2 = \frac{Z_1 Z_2 e^2}{b}; \text{ with } a = \frac{b}{2} = \frac{Z_1 Z_2 e^2}{\mu v} \text{ and } \mu = \frac{M_1 M_2}{M_1 + M_2}. \quad (6)$$

The variables Z_1 , Z_2 , M_1 , M_2 and v retain their previous definitions, μ is the reduced mass and $e^2 = 1.44 \text{ MeV}\cdot\text{fm}$ in the centimetre–gram–second (c.g.s) system.

2.2 Basic Considerations

The basic assumption of Coulomb excitation is that the interaction between the target and projectile is purely electromagnetic, i.e., nuclear interactions can be neglected. For this condition to be realised, the maximum “safe” bombarding energy has to be well below the height of the Coulomb barrier [1, 8]. Studies of Coulomb-nuclear interference effects have been carried out to estimate the maximum “safe” bombarding energy, E_{max} , involving the masses and charges of the interacting nuclei [10]. The safe bombarding energies for any projectile and target combination can be calculated using the classical expression of the minimum distance separating the nuclear surfaces, $S(\vartheta)_{min}$, in equation 7. A $S(\vartheta)_{min} \geq 5.1 \text{ fm}$ for “safe” heavy-ion Coulomb excitation was prescribed by Cline [11], while Kean [9] and Spear [1] suggested a more conservative $S(\vartheta)_{min} \geq 6.5 \text{ fm}$, for measurements involving light nuclei.

$$S(\vartheta)_{min} = \frac{0.72 Z_1 Z_2}{E_{max}} \left(1 + \frac{A_1}{A_2}\right) \left[1 + \operatorname{cosec}\left(\frac{1}{2}\vartheta\right)\right] - 1.25(A_1^{1/3} + A_2^{1/3})\text{fm}, \quad (7)$$

where the nuclear radius is taken as $1.25A^{1/3} \text{ fm}$. A measure of the minimum distance, d_{min} , for which the excitation is purely electromagnetic can be calculated from the $S(\vartheta)_{min}$,

$$d_{min} \geq 1.25(A_1^{1/3} + A_2^{1/3}) + S(\vartheta)_{min}. \quad (8)$$

Furthermore, a simplified picture of the excitation process can be obtained through the semi-classical approximation assuming a hyperbolic trajectory of the projectiles and a quantum-mechanical treatment of the excitation.

2.3 Semi-Classical Approximation

The theory of Coulomb excitation is based on the semi-classical description of the projectile's orbit. In the semi-classical approximation, nuclear transitions are induced purely through the time-dependent electromagnetic field acting between the projectile and the target. The projectile moves along a classical hyperbolic trajectory in the presence of the target's Coulomb field as shown in Fig. 2. The use of this simplified picture is justified if:

1. The motion of the projectile with velocity, v , is characterised by the Sommerfeld parameter (η), which is the ratio of the half distance of closest approach in a head-on collision, a , to the de Broglie wavelength (λ) of the projectile. The following condition must be fulfilled for a semi-classical treatment,

$$\eta = 2\pi \frac{a}{\lambda} = \frac{Z_1 Z_2 e^2}{\hbar v} \gg 1. \quad (9)$$

If this condition is met, the measurement is said to be free of nuclear interferences [1].

2. The energy transferred by the projectile, $\Delta E_{if} = E_i - E_f$, during collision with the target should be small compared to the bombarding energy, $E_{CM} = \frac{1}{2}\mu v^2$, i.e., $\frac{\Delta E_{if}}{E_{CM}} \ll 1$. If this condition is met, then it can be assumed that the energy transfer during the collision does not modify the classical trajectory significantly, and the energy loss during excitation may be neglected [8, 10].

Another important aspect of the Coulomb-excitation reaction is the time interval during which an appreciable torque acts on the nucleus and how this time compares with the lifetime of the nuclear state being excited. The extent to which the collision process is adiabatic or of sudden impact can be expressed using the dimensionless quantity ξ , called the adiabaticity parameter and is defined by,

$$\xi = \frac{t_{coll}}{\tau} = \frac{a\Delta E}{\hbar v}, \quad (10)$$

where the lifetime of the nuclear level can be calculated using the uncertainty principle,

$$\tau = \frac{h}{\Delta E}, \quad (11)$$

and the collision time is given by,

$$t_{coll} = \frac{a}{v}. \quad (12)$$

Values of $\xi \lesssim 1$ correspond to sudden impact collisions, whereas for $\xi > 1$ the collision is adiabatic. Accordingly, the Coulomb-excitation cross section is enhanced for $\xi \ll 1$ values and decays exponentially for $\xi \gtrsim 1$ values.

In the semi-classical approach, the Rutherford differential cross-section associated with the projectile's motion can be described by the well-known expression,

$$d\sigma_R = \frac{1}{4} a^2 \left(\sin \frac{\vartheta}{2} \right)^{-4} d\Omega. \quad (13)$$

If during the collision, the nucleus undergoes a transition from the ground state $|i\rangle$ to the final state $|f\rangle$, the Coulomb excitation cross-section may be related to the Rutherford cross-section by,

$$d\sigma_f = P_{if} d\sigma_R, \quad (14)$$

where P_{if} is the probability that a nucleus is excited in a collision in which the particle is scattered into the solid angle $d\Omega$. The probability P_{if} is expressed as,

$$P_{if} = \frac{1}{2I_i + 1} \sum_{M_i M_f} |b_{if}|^2, \quad (15)$$

where b_{if} are the transition amplitudes for excitation of a nucleus from the ground state with spin I_i to the final state I_f . M_i and M_f are the magnetic substates quantum numbers of the initial and final states, respectively. Perturbation treatment of the semi-classical approximation provides an understanding of the excitation process. P_{if} for light-ion Coulomb excitation is less than unity, hence, a first-order perturbation treatment of the excitation process may be adequate. The use of heavy targets, however, enhances second and higher-order terms in the perturbation expansion of the Coulomb-excitation cross section.

Magnetic transition amplitudes are hindered by a factor v/c compared with electric transitions of the same multipole order, and are, therefore, neglected in the perturbation treatment.

In this simplified model, quantum effects on the motion of the projectile are neglected. This may cause deviations from calculations of a factor of about $1/\eta$. Light-ion Coulomb excitation is associated with $\eta \gtrsim 1$ and increases to ranges of about 10^3 for heavy-ions. Deviations may be improved by substituting the particle velocity v with some mean value between the projectile initial and final velocities, v_i and v_f , respectively, leading to the symmetrized formulas for a and ξ ,

$$a_{if} = \frac{Z_1 Z_2 e^2}{\mu v_i v_f}, \quad (16)$$

and

$$\xi_{if} = \frac{a \Delta E}{\hbar} \left(\frac{1}{v_f} - \frac{1}{v_i} \right). \quad (17)$$

2.4 First-Order Perturbation Treatment

The excitation amplitudes of Coulomb-excited states can be evaluated using first-order perturbation theory when high-lying contributions or couplings are negligible. The first-order perturbation treatment of the cross-sections describes the interaction between the electromagnetic field and a system of nuclear charges. This approach has yielded reasonable estimates of the excitation amplitudes and cross sections for nuclei with final state $|f\rangle$, which are strongly coupled to the initial state $|i\rangle$ through a large matrix element, and the $|f\rangle$ state is not strongly coupled by its diagonal matrix element or any other high-lying states. This process is outlined in Fig. 3.

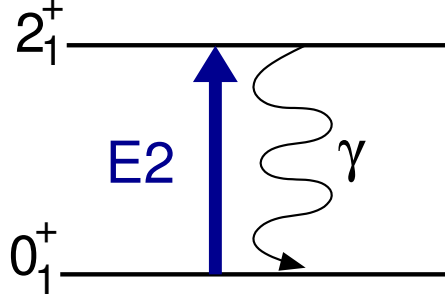


Figure 3: Schematic of first-order Coulomb excitation for an even-even nucleus from an initial state $|i\rangle$ to a final state $|f\rangle$ and its subsequent de-excitation by γ -ray decay.

The application of the first-order perturbation treatment to evaluate the excitation amplitude is only valid if the projectile-target interaction is weak, i.e., the excitation probability is small compared to unity. The excitation amplitudes obtained from first-order time-dependent perturbation theory may be expressed as,

$$b_{if}^{(1)} = \frac{1}{i\hbar} \int_a^b \langle f | H_{int}(t) | i \rangle e^{(i/\hbar)(\Delta E)t} dt, \quad (18)$$

where $H_{int}(t)$ is the monopole-multipole time-dependent interaction energy and

$$\Delta E = E_f - E_i \quad (19)$$

is the excitation energy for a transition from an initial state with energy E_i to a final state with energy E_f . The Coulomb energy responsible for electric multipole transition of order λ is explicitly defined in Ref. [10] as,

$$H_{int}(t) = 4\pi Z_1 e \sum_{\lambda=1}^{\infty} \sum_{\mu=-\lambda}^{\lambda} \frac{(-1)^{\mu}}{2\lambda+1} M(E\lambda, \mu) Y_{\lambda\mu}(\theta, \phi) \mathbf{r}^{-\lambda-1}, \quad (20)$$

where λ and μ are the multipole order of the excitation and the corresponding magnetic quantum number respectively, and $M(E\lambda, \mu)$ is the electric multipole operator, defined as,

$$M(E\lambda, \mu) = \int \mathbf{r}^{\lambda} Y_{\lambda\mu}(\theta, \phi) \rho(\mathbf{r}) d\tau, \quad (21)$$

where $\rho(\mathbf{r})$ is the nuclear charge density and $Y_{\lambda\mu}(\theta, \phi)$ represents the spherical harmonics. If the transition probabilities are small, one can employ first-order

perturbation to obtain the transition amplitudes. This is achieved by substituting equation 20 into equation 18, which yields,

$$b_{if}^{(1,1)} = \frac{4\pi Z_1 e}{i\hbar} (-1)^\mu S_{\mu\lambda} \langle I_i M_i | M(E\lambda, \mu) | I_f M_f \rangle, \quad (22)$$

where I and M are the nuclear states total angular momentum and magnetic quantum numbers, respectively, and

$$S_{\mu\lambda} = \int_{-\infty}^{\infty} e^{(i/\hbar)(\Delta E)t} Y_{\lambda\mu}(\theta(t), \phi(r)) \mathbf{r}(t)^{-\lambda-1} dt \quad (23)$$

is the time-dependent orbital integral. The reduced matrix elements of the electric nuclear moments can be defined using the Wigner-Eckart theorem with the aid of the Wigner 6 - j symbols,

$$\langle I_i M_i | M(E\lambda, \mu) | I_f M_f \rangle = (-1)^{I_i - M_i} \begin{pmatrix} I_i & \lambda & I_f \\ -M_i & \mu & M_f \end{pmatrix} \langle I_i || M(E\lambda) || I_f \rangle, \quad (24)$$

which only depends on the nuclear properties. The corresponding reduced transition probability may be written as,

$$B(E\lambda; I_i \rightarrow I_f) = (2I_i + 1)^{-1} |\langle I_i || M(E\lambda) || I_f \rangle|^2. \quad (25)$$

Finally, the Coulomb-excitation cross section for electromagnetic excitation may be expressed by,

$$\sigma_{E\lambda}^{(1)} = \left(\frac{Z_1 e}{\hbar v} \right)^2 a^{-2\lambda+2} B(E\lambda) f_{E\lambda}(\xi), \quad (26)$$

where λ represents the multipole order of the excitation. The values for the function $f_{E\lambda}(\xi)$ are tabulated in Ref. [10]. At small v/c values, magnetic contributions to the total cross-sections are suppressed compared to electric excitations ($E\lambda$) by a factor of β^2 and are, therefore, neglected in the perturbation treatment. The expression in equation 26 can be modified to account for magnetic transitions in relativistic Coulomb-excitation reactions Ref. [10]. The total Coulomb-excitation cross section expressed in equation 26 is directly proportional to the reduced transition probabilities expressed in equation 25. If the excitation amplitudes are large enough, it is possible to excite nuclear

states through a multiple-step process as shown in Fig 4. Under this condition, the excitation process deviates from first-order perturbation theory. Such deviations are corrected by extending the theory to second-order effects and using coupled-channel calculations.

2.5 Second-Order Perturbation Treatment

In the first-order perturbation theory, the excitation probability, P_{if} , in a single encounter is less than unity, making the use of semi-classical approximation justifiable. However, in heavy-ion Coulomb excitation, the collision of the projectile and the target can induce a two-step excitation or excitation of multiple nuclear states which are unreachable in a single-step first order perturbation theory. At this stage the P_{if} value may be equal or exceed unity. This excitation process can be described through the second-order perturbation theory. Here, a second (final) excited nuclear state $|f\rangle$ may be reached through excitation of an intermediate (first) state $|z\rangle$, from the ground state $|i\rangle$ followed by a transition from the intermediate state to the final excited state. The final excited state $|f\rangle$ may not be a third nuclear state lying at some energy ΔE above the intermediate state, it may arise from the excitation of the magnetic substates M_z of the first excited state $|z\rangle$ by itself as shown in Fig 4. This process is widely known as the reorientation effect because the magnetic substates rearrange themselves depending on the shape of the nucleus.

Furthermore, even when the probability, P , is small, it is still possible to observe higher-order effects if the direct transition from $|i\rangle$ to $|f\rangle$ is weak. By second-order perturbation treatment, the projectile's motion may again be described by semi-classical approximation. In this second-order treatment, the excitation amplitudes can be written as,

$$b_{if}^{(2)} = b_{if}^{(1)} + b_{izf}^{(1,2)}, \quad (27)$$

where $b_{if}^{(1)}$ and $b_{izf}^{(1,2)}$ represent the first-order and second-order amplitudes, respectively. In equation 27, $b_{if}^{(1)}$ is defined in equation 22 and represents the transition from the ground state to the intermediate state, while $b_{izf}^{(1,2)}$ represents the amplitude for the transition from the intermediate state to the final

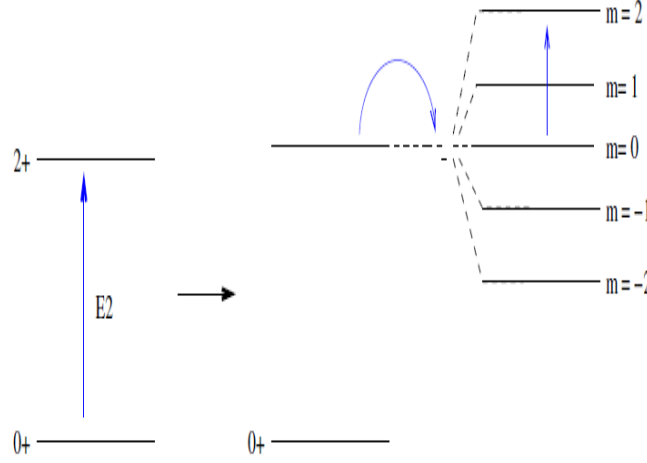


Figure 4: Schematic representation of the reorientation effect, a second-order effect in Coulomb-excitation perturbation theory. On the left, the nucleus is excited from the ground state to an intermediate state through a first-order or single-step process. On the right, final states involving the magnetic substates of the 2^+ state are populated through the reorientation effect.

state given by,

$$b_{izf}^{(1,2)} = (i\hbar)^{-2} \int_{-\infty}^{\infty} dt \langle f | H_{int}(t) | z \rangle e^{-\frac{E_f - E_z}{i\hbar} t} \int_{-\infty}^t dt' \langle z | H_{int}(t') | i \rangle e^{-\frac{E_z - E_i}{i\hbar} t'}. \quad (28)$$

The sum of the first order excitation amplitude $b_{if}^{(1)}$, defined in equation 22 extends over the complete set of intermediate states $|z\rangle$.

The excitation probability to second order may be calculated from the amplitude $b_{if}^{(2)}$. The excitation probability is composed of the term $P^{(1)}$, which contains only the first-order probability, an interference term $P^{(1,2)}$ between the first order and the second-order, and a term $P^{(2)}$ which contains only second-order amplitudes. It is thus written as,

$$P = P^{(1)} + P^{(1,2)} + P^{(2)}. \quad (29)$$

The term $P^{(1,2)}$, is only considered if the $P^{(2)}$ term is taken into consideration.

The total second-order differential cross-section may be written as;

$$d\sigma = d\sigma^{(1)} + d\sigma^{(1,2)} + d\sigma^{(2)} \quad (30)$$

where $d\sigma^{(1)}$, $d\sigma^{(1,2)}$ and $d\sigma^{(2)}$ represent the first-order differential excitation cross-section, the interference between first- and second-order excitations, and the second-order differential excitation cross section, respectively.

2.6 Coulomb excitation analysis: GOSIA

The development of a semi-classical approach for multiple Coulomb excitation [10] has come with advances in the analysis of Coulomb excitation experiments. This approach led to the first semi-classical multiple Coulomb excitation analysis computer program, COULEX, which was developed by Winther and de Boer [12]. The Winther and de Boer code played a vital role in the early analysis of Coulomb excitation experiments. The code uses a set of assumed initial matrix elements, level scheme and experimental details to calculate integrated γ -ray yields, which can be compared to the experimentally measured yields. Semi-classical coupled channel calculations have to be corrected to account for the transfer of energy to excite the nucleus and systematic errors. The errors in energy transfer are corrected by the use of the symmetrized orbits in the semi-classical calculations. An agreement between measurements and calculations can be accomplished by manually varying the model-dependent parameters. However, the model-dependency of the code proved to be of concern for many coupled states observed in multiple-step Coulomb-excitation measurements with heavy ions.

A model-independent semi-classical Coulomb excitation code, GOSIA, was instead developed [13]. The experiment-oriented program, GOSIA, modeled on the 1978 vision [14] of COULEX has the primary purpose to design and analyse experiments and fit matrix elements. It has been extensively used in the analyses of the Coulomb-excitation measurements described in this thesis. The code GOSIA extended the Winther and de Boer code to include not only the observed γ -ray yields, but also the branching ratios between states, lifetime of the states, the $E2/M1$ multipole mixing ratios and reduced matrix elements of multi-polarities, $\lambda = 1, 2, 3, 4, 5, 6$ for electric transitions and $M1$ magnetic transitions only. GOSIA is capable of fitting a maximum of 500 reduced matrix elements in a system of 75 levels. The information provided by the user

enables GOSIA to locate a fit which converges to yield the best χ^2 minimum value defined in equation 34. The χ^2 value depends on the difference between calculation and experiment. The GOSIA package comprises seven computer codes:

1. GOSIA \Rightarrow Designed to simulate and analyse $P-\gamma$ coincidence experiments and γ yields from Coulomb excitation experiments.
2. SIGMA \Rightarrow Quadrupole rotational-invariants fit code.
3. GOSIA2 \Rightarrow GOSIA variant code designed for measurement of the ratio of target and projectile excitation. The code normalises to the well-known matrix elements in the target. Typically used for radioactive ion beam experiments.
4. RACHEL \Rightarrow A GUI for GOSIA to facilitate and simplify GOSIA's extensive input and output.
5. PAWEL \Rightarrow GOSIA variant designed to handle an excited isomeric initial state.
6. ANNL \Rightarrow GOSIA variant that uses simulated annealing for the least squares fit.
7. GREMLIN \Rightarrow A code to fit γ -ray detection efficiency data.

However, the goal of this work is to extract diagonal matrix elements through the evaluation of excitation probabilities and γ -ray decay yields for a given set of matrix elements in the level scheme under consideration. The code GOSIA will be used for data analysis associated with this work. Although GOSIA is primarily used to calculate the magnitude of experimental observables, either for designing of experiments or for analysis of experimental data, experimentally inferred reduced matrix elements can also be compared to theoretical calculations in accordance to the rotational model formalism outlined by Bohr and Mottelson [15].

The initial input (OP,THEO) of GOSIA uses the previously known information (such as reduced matrix elements and quadrupole moment) to generate theoretical matrix elements in accordance to the geometrical rotor model [15]. In the second input and all succeeding input files, experiments are defined using the projectile's and target's protons (Z) and nucleons (A), the energy of the projectile, and the geometry of particle and γ -ray detectors. The investigation nucleus is further defined by a set of known matrix elements for each transition, lifetimes of each state, branching and mixing ratios. The experimentally measured integrated γ -ray yields Y_{exp} and their errors, are required by the second input file to calculate a new set of yields which correct for differences between the yields calculated using full integration (Y_{int}) and the point yields (Y_{point}) calculated using mean values of the bombarding energy ranging from E_{min} to E_{max} , scattering angle (θ_{min} , θ_{max}) and (ϕ_{min} , ϕ_{max}) in the laboratory frame. For each experiment, Y_{exp} , Y_{point} and Y_{int} are calculated using,

$$Y_{exp}^c(I_i \rightarrow I_f) = Y_{exp}(I_i \rightarrow I_f) \frac{Y_{point}(I_i \rightarrow I_f)}{Y_{int}(I_i \rightarrow I_f)}, \quad (31)$$

where

$$Y_{point}(I_i \rightarrow I_f) = \sin\theta_p \int_{\phi_p} \frac{d^2\sigma(I_i \rightarrow I_f)}{d\Omega_\gamma d\Omega_p} d\phi_p, \quad (32)$$

and

$$Y_{int}(I_i \rightarrow I_f) = \int_{E_{min}}^{E_{max}} dE \frac{1}{\left(\frac{dE}{dx}\right)} \int_{\theta_{p,min}}^{\theta_{p,max}} Y_{point}(I_i \rightarrow I_f) d\theta_p. \quad (33)$$

Equation 32 includes the Rutherford cross-section and the solid angle factor, $\sin(\theta_p)$. The electronic stopping powers, dE/dx , are obtained through the SRIM 2012 code [16], and using a spline interpolation given by a range of mesh points that accommodates the target thickness. When defining experiments, the first experiment will correspond to the lowest -most yields observed in a γ -ray detector. The numerical offset is corrected by renormalising in such a way that the corrected and actual yields are equal. This is possible since the absolute cross-section is not required by GOSIA, therefore, GOSIA always fits the matrix elements with at least one normalisation factor for all defined experiments. If the target is the same for all experiments, the renormalisation procedure becomes less complicated since the energy loss integration is the same for all experiments. The fitting of the matrix elements is performed by locating a χ^2

minimum in equation 34 of the experimental (actual) yields and the corrected yields,

$$\chi^2 = \frac{1}{N} \sum_i \left(\frac{Y_{exp}(i) - Y_{exp}^c(i)}{\Delta Y_{exp}(i)} \right)^2, \quad (34)$$

where $Y_{exp}(i)$, $\Delta Y_{exp}(i)$ and N represent the actual yields, error and number of data points (experiments), respectively. The minimisation process can be time consuming, so effective use of the parameters provided by the user may be useful for considerable time saving. The user may vary the matrix elements until the best χ^2 value is obtained [17]. An alternative way is to vary only a subset of the matrix element and fixing some matrix elements with weak influences in the population of the state of interest.

The final stage involves the evaluation of the error bars to be assigned to the determined matrix elements corresponding to the χ^2 value. To simplify this process GOSIA uses a two step method. The first is the calculation of diagonal (uncorrelated) errors for all matrix elements. When calculating diagonal errors, GOSIA fixes all but one of the matrix elements until all errors are evaluated. The errors are obtained by sampling the χ^2 value for different values of matrix elements in the vicinity of the minimum. This step is useful for identifying matrix elements which still lie far from the fit and is (the step) separated from the full (correlated) calculation of errors, which is the last step. Calculation of correlated errors requires the diagonal errors, this step generally increases the error bars as it includes the dependence on the other matrix elements. When calculating the correlated errors, GOSIA performs an integral along the axis of maximum correlation found by partial minimisation. For a full overview of the GOSIA code, the user is referred to the GOSIA manual [13].

Chapter 3

3 Experimental Facility and Setup

In this chapter, experimental details of the Coulomb-excitation measurements performed in this work and the equipments used are discussed. The iThemba Laboratory for Accelerator Based Science (iThemba LABS) facility accelerators and the AFRican Omnipurpose Detector for Innovative Techniques and Experiments (AFRODITE) array are also discussed.

3.1 iThemba LABS Cyclotron Accelerator Facilities

At iThemba LABS, pre-acceleration of the beam ions is done through two solid-pole injector cyclotrons (SPC's). The first injector cyclotron (SPC1) pre-accelerates proton to maximum energy of 8 MeV. Low intensity beams of light and heavy-ions as well as polarised protons are pre-accelerated in a second injector cyclotron (SPC2) with a $K = 8$. The pre-accelerated beams are then send to the separated sector cyclotron (SSC), which is the main accelerator [18, 19], consisting of four 34° radial magnet sectors, with a total weight of 1,300 ton, a diameter of 13.2 m and a height of 7 m have been positioned to an accuracy of 0.1 mm.

The SSC is a $K = 200$ machine. Fig 5 shows the iThemba LABS SSC facility. The vacuum chambers of the magnets are mounted in the pole gaps with the 29 trim coils, for isochronisation of the magnetic field, outside the vacuum system in the gaps between the poles and the vacuum chamber walls, thereby eliminating the need for hundreds of water and power feed-troughs [18, 19].

Two $\lambda/2$ -resonators, capacitively coupled through 50 ohm cables to 150 kW power amplifiers provide a maximum dee voltage of 220 kV in the frequency range of 6 to 26 MHz [19]. The injection system of the SSC consists of two bending magnets and a magnetic inflection channel. The beam is extracted with two septum magnets. An electrostatic extraction channel is also available for extraction but has seldom been used, since the large spaces between magnet sectors allow operation with high dee voltages and good orbit separation

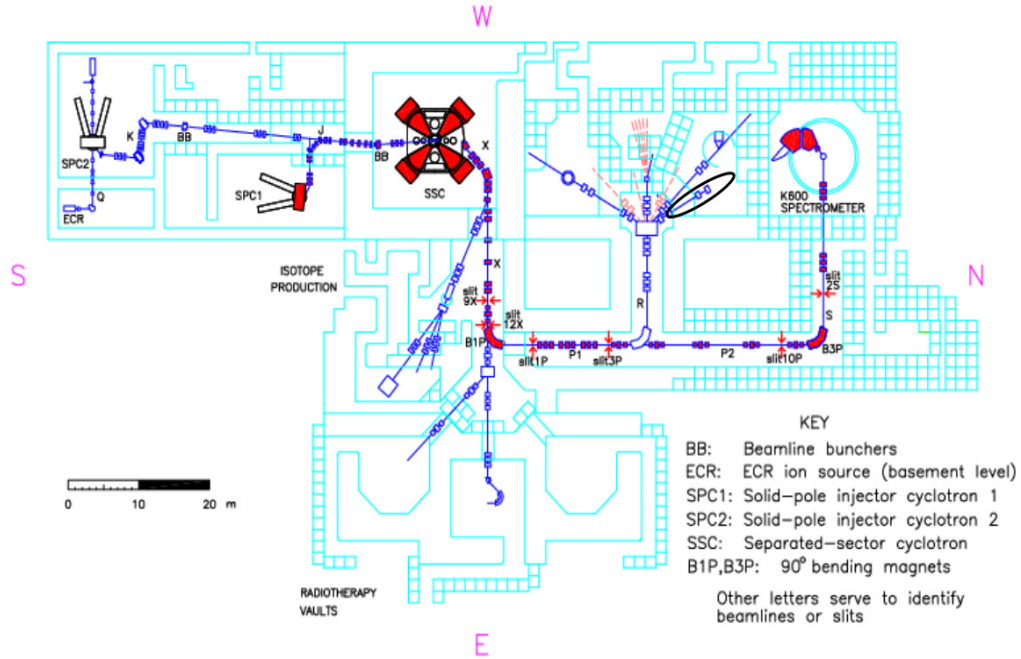


Figure 5: The iThemba LABS facility.

at extraction. The sharp drop-off in the magnetic field at the extraction radius, due to the small pole gap, and the relatively large spaces available for extraction components in the two valleys between magnet sectors not occupied by resonators allows much easier beam extraction than in the case of solid-pole cyclotrons. The SSC accelerates beams of light and heavy-ions as well as beams of polarized protons.

3.1.1 The AFRODITE Array

AFRODITE is a medium size γ -ray spectrometer array that has the unique capability of detecting both high and low energy photons with a reasonably high efficiency. The array consists of nine large volume escape suppressed HPGe Clover detectors (five at 90° and four at 135°) and eight Low Energy Photon Spectrometer (LEPS) detectors in its full form. These detectors are mounted around the AFRODITE rhombicuboctahedron frame. Each Clover detector consists of four $50 \times 50 \times 70 \text{ mm}^3$ HPGe crystals and the nine Clovers subtend 11% of $4\pi \text{ Sr}$. The Low Energy Photon Spectrometers consist of four segmented planar Ge detectors of $2800 \text{ mm}^2 \times 10 \text{ mm}$ volume.

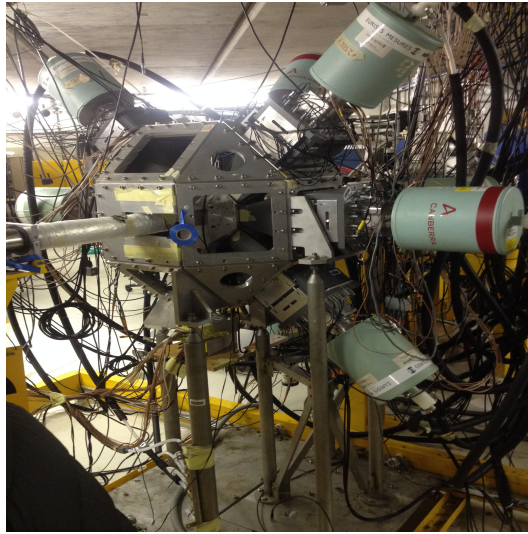


Figure 6: *The geometry of the AFRODITE array with 8 clover detectors placed at θ_{lab} of 90° and 135° along the beam line.*

At the center of the array, a 16 square faces target chamber of the same geometry is fitted as illustrated by Fig 6. The AFRODITE detectors need to be maintained at liquid nitrogen temperatures of approximately -198°C . The detectors are filled by an automated liquid nitrogen cooling system, the temperatures are monitored by a PC with the required analogue- and digital I/O cards. For the purpose of this work, only eight clover detectors (five at $\theta_{lab} = 90^\circ$ and three at $\theta_{lab} = 135^\circ$) and no LEPS detectors were used in conjunction with a double-sided silicon particle detector mounted inside the target chamber. The distance between the center of the target chamber and the front face of each clover detector was 19.6 cm.

3.2 Detector Systems

The use of semiconductor junction diodes as radiation detectors for particle and γ -ray detection has provided nuclear physicists with solutions to achieve accurate measurements due to improved energy resolution. In semiconductor detectors, charged particles and γ -ray are identified through direct collection of primary ionisation and measurement of the energy of nuclear radiation (particle or γ ray) [20]. Incident radiation creates electron-hole pairs when interacting with the detector provided enough energy is supplied to the semiconductor crys-

tal. The electron-hole pairs serve as the fundamental carriers of information. The number of electron-radiation pairs created when radiation interacts with the detector is proportional to the supplied energy. The most common semiconductor materials used for constructing this type of detectors is Germanium (Ge) and silicon (Si). For a more in depth review of these radiation detector, the reader is advised to visit Ref. [20, 21], as this work will only give a brief discussion on the detectors used for this work.

3.2.1 High purity germanium (HPGe) clover Detectors

High purity germanium (HPGe) detectors are a class of semiconductor diode based detectors used for γ spectroscopy in nuclear structure research. The detectors first became available in the mid 70's, and came about with significant improvements in nuclear research due to their excellent resolution and energy stability [22]. The detectors are normally maintained at liquid nitrogen temperature (77K).

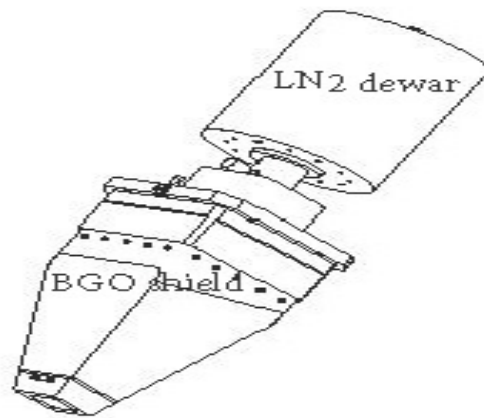


Figure 7: *The schematic representation of a clover detector with the BGO shield and cylindrical liquid nitrogen (LN_2) dewar.*

HPGe clover detector, shown in Fig 7 is made of four N-type crystals (with a diameter of 5.1 cm and length of 7 cm individually) packed together in four quadrants of a square and housed in a cryostat. As shown in Fig 8, the crystals are closely packed in the front with a crystal-crystal distance of 0.2 mm and retains about 89% of the original crystal volume. Each crystal has a square front face with round edges obtained by tapering it on two adjacent faces with

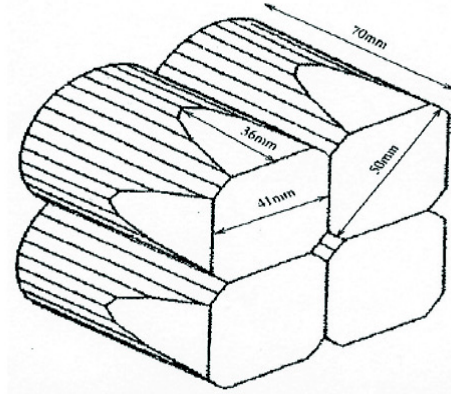


Figure 8: *The schematic view of the four segments of a HPGe clover detector and its dimensions.*

an angle of 7.1° starting at around the half of the length and by cutting the two remaining faces parallel to the crystal axis and along its whole length. The close packing of the crystals increases the probability of detecting a Compton scattered γ -ray from the neighboring crystal.

3.2.2 Addback

The total photopeak efficiency of any γ ray detected within a detector with more than one crystal (segment) includes the effect of two complimentary processes:

1. Single fold events; when full γ ray energy is deposited in any one of the individual crystals, efficiency can be obtained directly from individual crystals.
2. Coincidence detection; when the γ ray is Compton scattered from one crystal to an adjacent crystal of the same clover detector the full γ -ray energy will result from the partial absorption in two or more crystals through Compton effect (and/or pair production process followed by escape of one/both of the 511 keV γ rays for high energy photons). In this mode, energy signals of individual crystals are simultaneously produced and recorded event by event in the list mode. The energy detected in both segments can be added to obtain the full energy of the γ ray. This process

is known as “addback”. The efficiency is determined from the addback spectra. This enhance the photopeak efficiency of the clover detectors especially for the γ rays with high energy.

The efficiency of this composite detector is;

$$\epsilon_{total} = \epsilon_{direct} + \epsilon_{addback}, \quad (35)$$

and the addback factor F is defined as the ratio of the total full energy peak efficiency to the direct detection efficiency;

$$F = \frac{\epsilon_{total}}{\epsilon_{direct}}. \quad (36)$$

In clover detectors, at around $E_{gamma} = 1$ MeV, the addback improves the absolute efficiency by about a factor of 1.5. However, this ratio is energy dependent. At low energies, where Compton scattering is not dominant, single fold events will have more influence on the absolute efficiency.

3.2.3 Compton Suppression

In the preceding section, the possibility for a γ -ray to Compton scatter and deposit only a fraction of its full energy was mentioned. The γ -ray may Compton scatter out of the germanium detector volume. This affects the quality of the data since the deposited partial-energy will contribute to a continuum distribution seen as background events. The number of partial-energy events in the spectrum can be reduced by Compton suppression. To accomplish this, a clover detector is surrounded a secondary detector, usually a scintillator detector. The most commonly used scintillator materials used for this purpose is bismuth germanate oxide ($\text{Bi}_4\text{Ge}_3\text{O}_{12}$), abbreviated as BGO. The BGO’s high Z value increases the likelihood of a γ -ray to interact with it. If a γ -ray is simultaneously (depending on timing conditions) detected by a crystal of the clover detector and the BGO shield, then it is interpreted as a scattering event and rejected from the data stream [22–24]. A heavy metal collimator (with 97% of it is being Tungsten) is installed in front of the BGO shield to prevent interaction between the BGO and γ rays coming directly from the target position. Fig 7 also shows the BGO suppression shield with the collimator in front of it.

3.2.4 Double-Sided S3 Silicon Detector

24 rings on the junction side and 32 sectors on the ohmic side. The CD-type S3 detector is a micro-strip detector resembles a compact disc (But with different dimensions). It has an inner diameter of 22 mm and an outer diameter of 70 mm with 24 annular strips (rings) of width 1 mm on the junction side and 32 sectors (subtending 11.25° degrees each) on the ohmic side [25,26]. Fig 9 shows the dimensions of the detector. In Fig 9, the two left-hand quadrants show the 24 annular strips on the junction side of the detector. The top right quadrant of the schematic shows the back view of the detector with its sectors, while the bottom right quadrant shows how the quasi pixels are formed by the overlap of the junction side and the ohmic side strips. The detector is capable of detecting

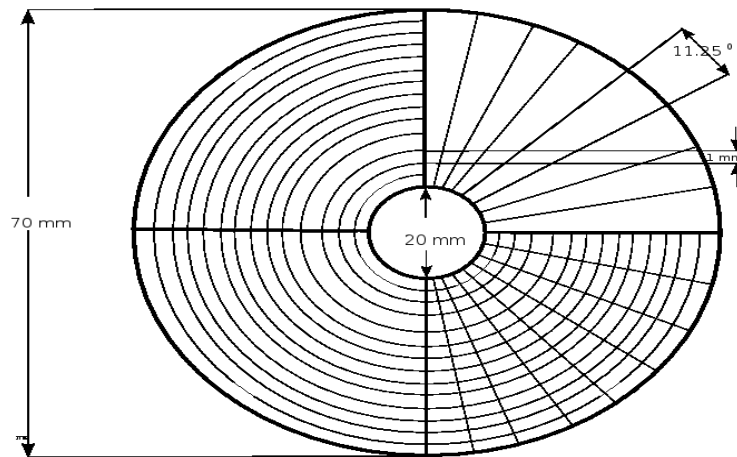


Figure 9: *The dimensions of an S3 detector.*

a charged particle (having energy E) and registers the position which was hit by the particle as it has discrete silicon micro-strips (pixels). Each pixel gives its own readout through which a signal can be observed. When a particle hits the detector, two concurrent signals with the same energy are produced: one from a ring on the junction side and one from a sector on the ohmic side. The two layers of strips are orthogonal with respect to each other, and the particle's position information is two dimensional. Adjacent pixels are separated by a thin dead-layer, which represents the inactive part (site) of the detector. It is possible for a particle to deposit some or all of its energy on the a dead-layer or on adjacent pixels. If a particle deposits all of its full range energy on the inactive site, the

Table 1: Geometry of the S3 silicon detector: ring #1 corresponds to the innermost ring and ring #24 corresponds to the outermost ring.

Ring#	R_{Min}	R_{Max}	R_{Av}	θ_{Min}	θ_{Max}	θ_{Av}
	mm	mm	mm	deg	deg	deg
1	11.5	12.4	11.9	131.2	129.1	130.1
2	12.5	13.4	12.9	128.9	127.0	127.9
3	13.5	14.3	13.9	126.8	125.0	125.9
4	14.4	15.3	14.9	124.8	123.3	124.0
5	15.4	16.3	15.9	123.1	121.6	122.4
6	16.4	17.3	16.9	121.5	120.2	120.8
7	17.4	18.3	17.8	120.0	118.8	119.4
8	18.4	19.3	18.8	118.7	117.6	118.1
9	19.4	20.3	19.8	117.4	116.4	116.9
10	20.4	21.2	20.8	116.3	115.3	115.8
11	21.3	22.2	21.8	115.2	114.3	114.8
12	22.3	23.2	22.8	114.2	113.4	113.8
13	23.3	24.2	23.8	113.3	112.6	112.9
14	24.3	25.2	24.7	112.5	111.8	112.1
15	25.3	26.2	25.7	111.7	111.0	111.3
16	26.3	27.2	26.7	110.9	110.3	110.6
17	27.3	28.1	27.7	110.2	109.7	109.9
18	28.2	29.1	28.7	109.6	109.0	109.3
19	29.2	30.1	29.7	109.0	108.5	108.7
20	30.2	31.1	30.7	108.4	107.9	108.2
21	31.2	32.1	31.6	107.9	107.4	107.6
22	32.2	33.1	32.6	107.3	106.9	107.2
23	33.2	34.1	33.6	106.9	106.4	106.6
24	34.2	35.0	34.6	106.4	106.0	106.2

energy readout corresponding to the detected particle is zero. If the particle deposit a fraction of its full range energy on adjacent pixels, charge (energy) sharing play a major role on acceptance of the detected particle. The term charge sharing refers to the result of the lost energy being collected by adjacent pixels, and this shared charge may give rise to double counts in adjacent pixels. These effects and possibilities will be reviewed in the next section. In Table 1, the 24 rings are numerically labeled from 1 to 24 with ring1 being the innermost ring and ring24 the outermost ring. The 32 sectors are numbered from 1 to 32. In the case of the sectors, the starting point is arbitrary. As shown in Fig 9, the detector has a hole in the center. The primary function of that hole is to let the beam through. The detector is called double-sided because of the two discrete pixel arrays on its junction- and ohmic side.

3.3 Data Acquisition System and Electronics

In order to utilize the AFRODITE array to its full capacity, the iThemba LABS facility makes use of a full digital data acquisition systems (DDAS) covering all the aspects of the array. The block diagram of the electronic setup with the data acquisition system is showed in Fig 10. For the current work, eight clover detectors were used for γ -ray detection of the de-excited γ rays. Each clover detector provides four channels corresponding to each crystal. This adds-up to 32 channels for all cover detectors. Furthermore, an extra channel per clover is used for anti coincidence with the BGO's. The γ -ray signals are integrated and amplified by the the built in two stage preamplifiers of the clover detector. The signal is then fed to the data acquisition system (DGF Pixie-16) where they are digitised. For the purpose of this work, six DGF Pixie-16 modules were housed on two separate PXI crates. The first crate was loaded with four Pixie-16 modules for collection of γ signals while the second crate contained four Pixie-16 for collection of particle signals from the S3 detector. The digitised γ and particle signals are then processed in a field-programmable gate arrays (FPGA) to obtain energy and timing information. The block diagram of the DDAS modules connection to the detectors may also be seen in Fig 10.

Signals from the S3 detector, which was powered by an MHV-4 bias unit shown in Fig 11, go through vacuum read through cables to two MPR-32 multichannel preamplifier shown in Fig 12. The top preamplifier used for 32 signals from the sectors and the bottom preamplifier accepted the signals from the 24 rings, leaving eight channels unused. The digitised particle and clover signals are collected at the same sampling frequency of 100 MHz. This is necessary since the particles and γ -rays are collected in coincidence. During the event building process, only γ -rays and particles with stamps of about 347 ns are registered. The time gate signal is predetermined by the RF. The acquired data are then sent to a PC running MIDAS (software) data acquisition system, where data are merged, filtered, built and stored. A schematic of the DDAS setup is shown in Fig 10.

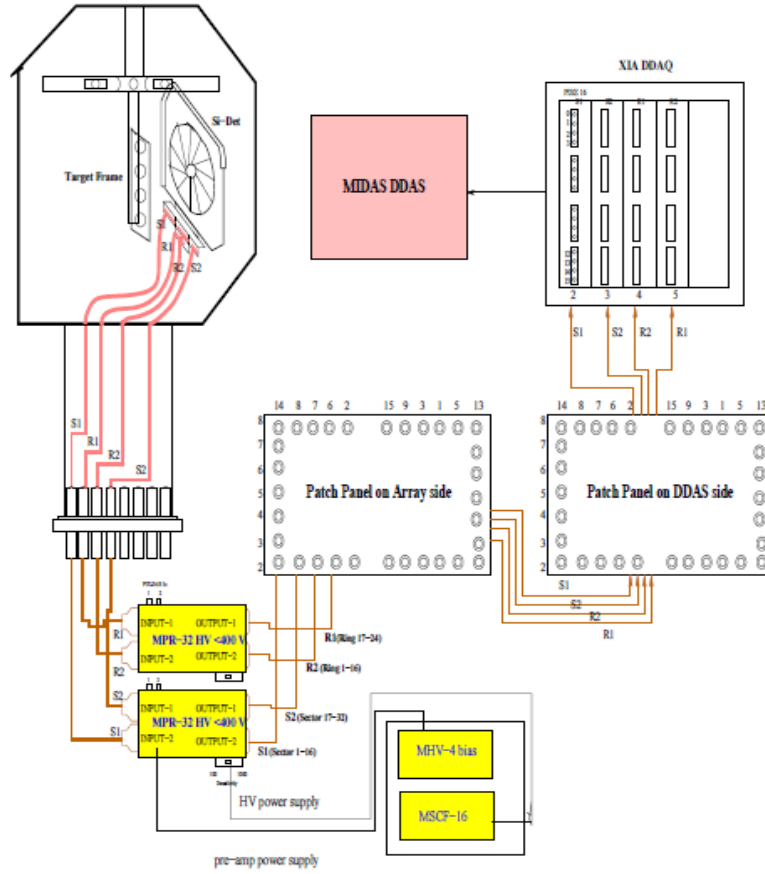


Figure 10: Schematic diagram showing the connections of detector systems to the AFRODITE patch panels and the DDAS.

3.4 The Coulomb Excitation Experiment

The 2_1^+ excited state in ^{40}Ar was populated through Coulomb excitation at iThemba LABS using the $^{208}\text{Pb}(^{40}\text{Ar}, ^{40}\text{Ar}^*)^{208}\text{Pb}^*$ reaction at the safe bombarding energy of $E_{lab} = 143.2$ MeV.

The energy of the beam and the Sommerfeld parameter η were calculated prior to experimental measurements using equation 7 and equation 9 respectively. The Sommerfeld parameter of $\eta \approx 134.4$ was obtained for the reaction concerning this work. Fig 13 shows the $S(\vartheta)_{min}$ at backward angles for $E_{lab} = 143.2$ MeV. This bombarding energy was minimised to enhance Coulomb population of the 2_1^+ get chosen to satisfy Spear's safe condition [1].

The scattered particles resulting from the elastic and inelastic collision of the

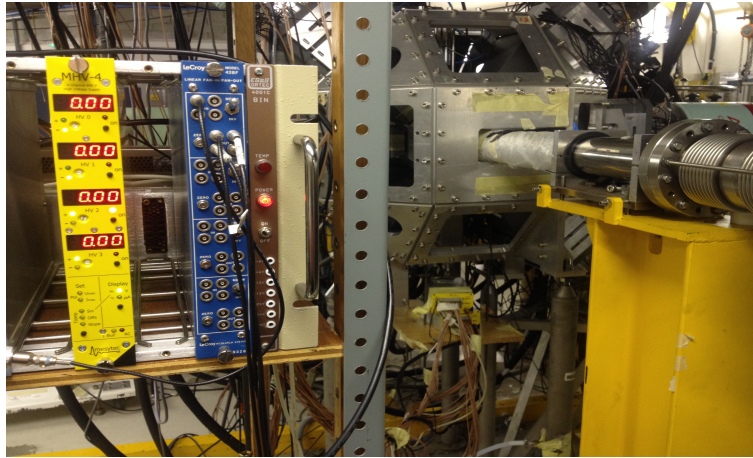


Figure 11: MHV-4 bias unit and timing filter amplifier.

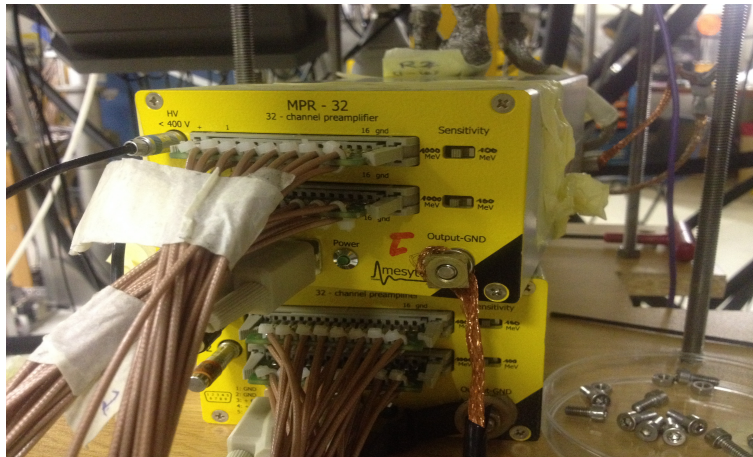


Figure 12: MPR-32 multichannel preamplifier of the S3 detector.

Table 2: Geometry of the AFRODITE array clover detectors

Clover	$\theta(deg)$	$\phi(deg)$
A	90	22.5
B	90	67.5
C	90	157.5
D	90	202.5
E	90	337.5
F	135	112.5
G	135	202.5
H	135	292.5

two nuclei were detected at backward angles with an S3 silicon detector and the de-excited γ rays were detected with the AFRODITE array equipped with

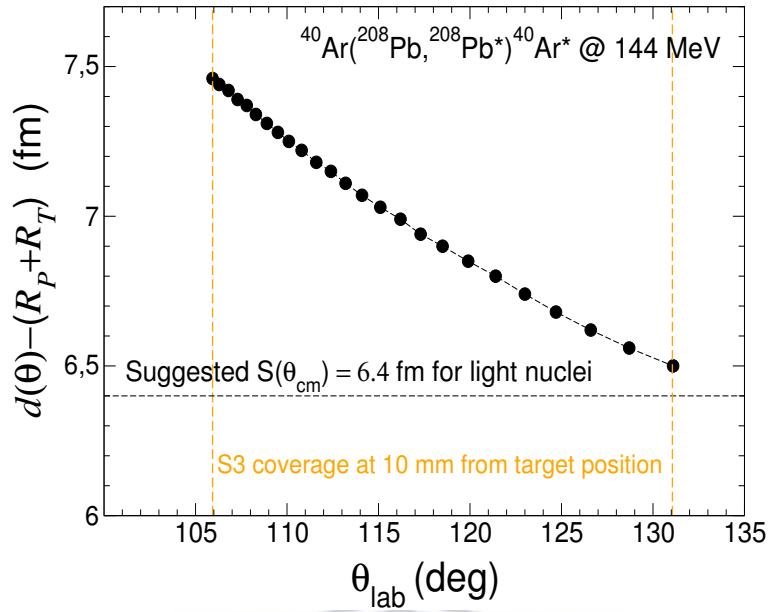


Figure 13: Plot of the $S(\vartheta)$ at different scattering angles θ .

Table 3: Summary of experimental details.

Projectile	^{40}Ar
charge state	+6
Beam energy	143.2 MeV
Beam current	0.5 nA
target	^{208}Pb
Target thickness	1.39 (0.01) mg/cm ²
Pulse selection	1 in 3
RF Pulse	197 ns

the eight clover detectors. Fig 14 shows the charged particle detector protected by two collimators and the target ladder. The ^{40}Ar beam delivered by the K = 200 SSC is tunned onto a beam viewer (ruby diamond) with a 3 mm hole in the middle. The ruby is viewed through a digital camera window of the AFRODITE scattering chamber. Once the beam had been focused and confirmed to be going through the hole of the ruby, it was then put through onto the ^{208}Pb target. The summary of the experimental details is given in Table 3. The energy loss in Table 4 was calculated for each ring for projectile traveling apparent thickness, t , within the target material. Thorughout the calculation of all values in Table 4, it was assumed that the interaction takes place in the middle of the target.

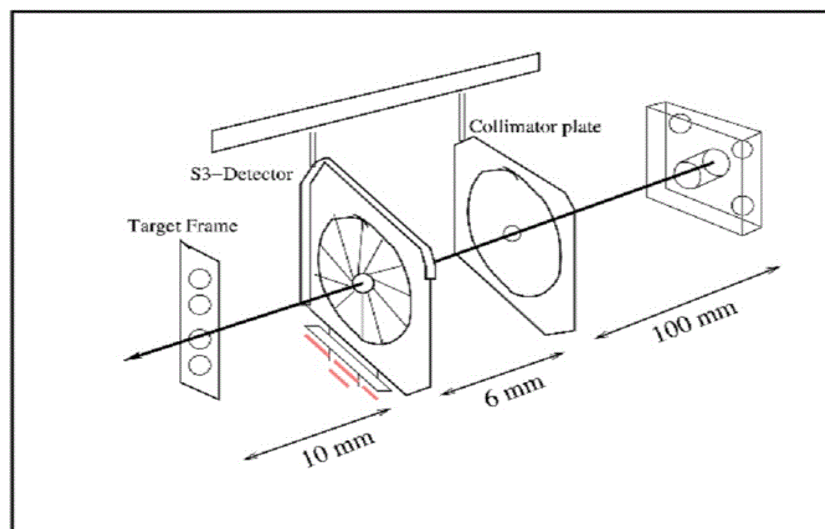


Figure 14: Schematic of the S3 particle detector placed at backward angles with two collimator placed on the front side of the rings in front of the rings and a target frame in front sectors.

Table 4: Energy loss of $^{40}\text{Ar}^{6+}$ ions impinging on ^{208}Pb at 143.2 MeV. θ_{min} and θ_{max} denote the minimum and maximum scattering angle in the laboratory frame for each ring, respectively, d and dE denote the thickness of the target and average energy loss through a target of thickness d .

Ring#	$\theta_{min}[deg]$	$\theta_{max}[deg]$	$d[\text{mg}/\text{cm}^2]$	$dE[\text{MeV}]$	$E - dE[\text{MeV}]$
1	131.2	129.1	1.078	7.2	131.3
2	128.9	127.0	1.13	7.6	131.0
3	126.8	125.0	1.19	7.9	130.6
4	124.8	123.3	1.24	8.3	130.2
5	123.1	121.6	1.30	8.7	129.9
6	121.5	120.3	1.36	9.1	129.5
7	120.2	118.8	1.42	9.5	129.1
8	118.7	117.6	1.48	9.9	128.7
9	117.4	116.4	1.54	10.3	128.3
10	116.3	115.3	1.60	10.7	127.9
11	115.2	114.3	1.66	11.1	127.5
12	114.2	113.4	1.72	11.5	127.0
13	113.3	112.6	1.78	11.9	126.6
14	112.5	111.8	1.86	12.3	126.2
15	111.7	111.0	1.91	12.8	125.8
16	110.9	110.3	1.97	13.2	125.4
17	110.2	109.7	2.04	13.6	124.9
18	109.0	109.0	2.10	14.1	124.5
19	109.0	108.5	2.17	14.5	124.1
20	108.4	107.9	2.23	14.9	123.6
21	107.9	107.4	2.30	15.4	123.2
22	107.3	106.9	2.36	15.8	122.8
23	106.9	106.4	2.43	16.2	122.3
24	106.4	106.0	2.50	16.7	121.9

Chapter 4

4 Data Analysis and Results

4.1 Interaction of Ions with Matter

In typical Coulomb-excitation reactions, energetic ion beams moving at speeds of about 10% percent the speed of light interact with a stationary target nucleus through the electromagnetic force. However, in the passage through the target, the projectiles interact with the atomic electrons and nuclei of the target material and thus causing energy deposition bringing about energy loss. The Bethe-Bloch formula in equation 37 gives the mean rate of energy loss (stopping power, dE/dx) for a heavy charged particle, $M_t \gg$ the mass of an electron (M_e),

$$-\frac{dE}{dx} = \left(\frac{Z_p e^2}{4\pi\epsilon_0}\right)^2 \left(\frac{4\pi Z_t \rho_t N_A}{A_t M_e v^2}\right) \left[\ln\left(\frac{2M_e v^2}{I_E}\right) - \ln(1 - \beta^2) - \beta^2 \right], \quad (37)$$

where A_t and ρ_t are the nuclear mass and density of the target material, respectively, while $I_E \approx 11Z_t$ eV is the mean energy required to ionise an atom of the target material. The most important features of equation 37 is the relationship between the energy loss, dE/dx , and the projectile atomic number, Z_p , which shows that projectiles with higher Z will be subject to a greater energy loss dE/dx than a low- Z projectile, i.e., the energy loss dE/dx is proportional to the square of the atomic number (Z^2) of the projectile.

The average energy loss calculation for the present work were carried out using SRIM 2012 [27]. The SRIM stopping power program calculates the energy lost by the projectile moving through a target of thickness $t = 1$ mg.cm² in a straight line. However, within the scope of Coulomb excitation, projectile is assumed to follow a hyperbolic trajectory discussed in Sec 2.1 and Sec 2.3. This path causes the projectile to travel an effective thickness, d , to escape the target material. The actual thickness, t , of the target and the effective thickness d traveled by the projectile (assuming a vertex point with two straight lines) before escaping the target material relate by the expression,

$$d = \frac{t}{\cos\theta}. \quad (38)$$

Fig 15 shows an incoming projectile recoiling in the middle of the target after traveling a thickness $t/2$ and escaping after traveling a thickness d at a backward angle θ . In calculating the energy loss of the projectile, it is convenient to

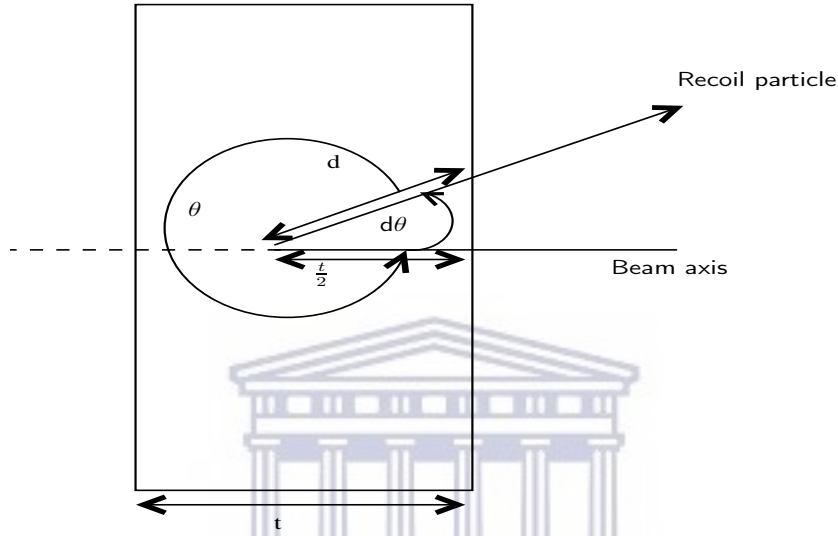


Figure 15: Interaction of projectile with target of thickness t : d denotes the effective thickness traveled by the projectile from the center of the target when scattered through an angle θ . $\frac{t}{2}$ is the interaction point in the middle of the target and $d\theta$ is the complimentary angle.

consider the particle as having traveled through a target of thickness

$$d_e = \frac{t}{2} + d. \quad (39)$$

In order for the particle to escape the target material after interaction, its range in the target should exceed the thickness, d , otherwise it will be stopped in the target. The energy loss used in this work are given in Table 4.

4.2 Detectors Energy and Efficiency Calibration

In order to perform the off-line data analysis, an accurate energy calibration for both the HPGe clover detectors and the S3 particle detector were carried out. In order to perform proper energy and efficiency calibrations, radiation sources of well-known energies and intensities are required.

4.2.1 Calibration of AFRODITE HPGe Clover Detectors

The AFRODITE arrays clover detectors were calibrated using a ^{152}Eu γ -ray source data collected before and after the experiment. The ^{152}Eu source was placed in-front of each hemisphere of the AFRODITE array such that all the detectors can detect the emitted γ rays collected on singles mode through the MIDAS software [28]. A MIDAS and MTsort [29] based off-line sorting code [30] were used to generate an uncalibrated ^{152}Eu γ ray spectrum which was then calibrated using the auto-calibration option in the MIDAS software to obtain the on-line calibrated ^{152}Eu γ ray spectrum (with a 1 keV/channel correspondence) shown in Fig 16. The drawback of the auto-calibration method lies in its inability to identify all the ^{152}Eu transitions. A manual calibration was performed to obtain the channel number of the unidentified transitions and the resulting gain and offset coefficients were then input into a off-line sort code to generate the spectrum in Fig 16.

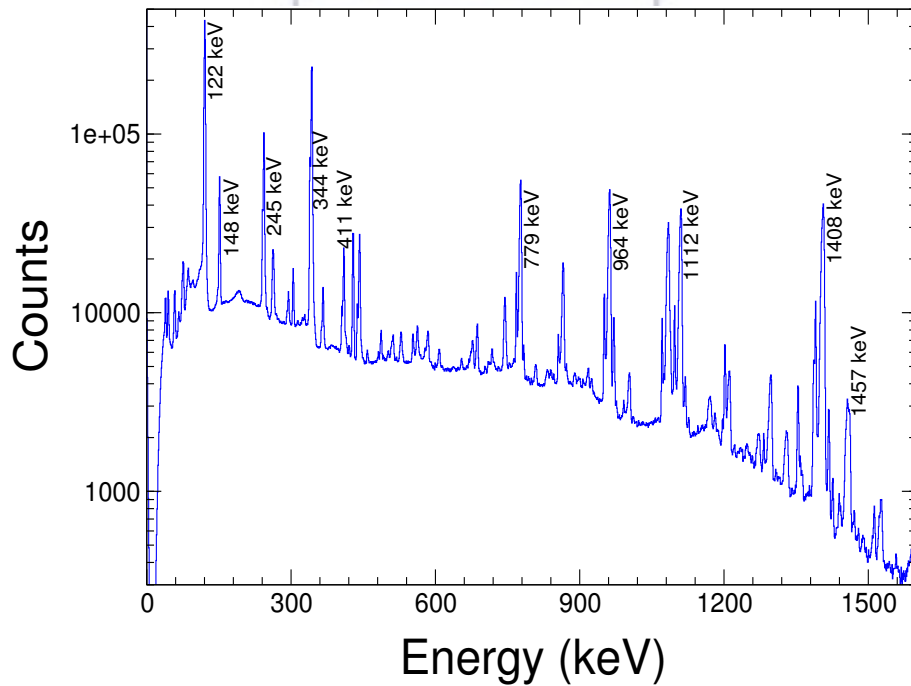


Figure 16: The ^{152}Eu source spectrum used for energy calibration. The most intense peaks are labeled.

4.2.2 Gamma Efficiency Calibration

In this analysis it is necessary to compare the intensities of γ -ray lines at different energies. In order to correct for efficiency at each reported energy it is of paramount importance to compare the intensities of γ -ray lines at different energies. The efficiency calibration (correction) measurements were also carried out using ^{152}Eu source full energy spectrum. To perform accurate efficiency calibration the ^{152}Eu source was placed at the target position.

The data were sorted off-line with a sorting code containing energy calibration coefficients using MIDAS, MTsort package. The output spectrum file was then analysed with the RADWare program, gf3 [31], which was used to obtain the area of each peak of the spectrum. This is done by using the gf3 FT command to fit the peaks for a Gaussian curve or the SB command if the peak is not a perfect Gaussian curve. These areas are then stored in a .sto file which

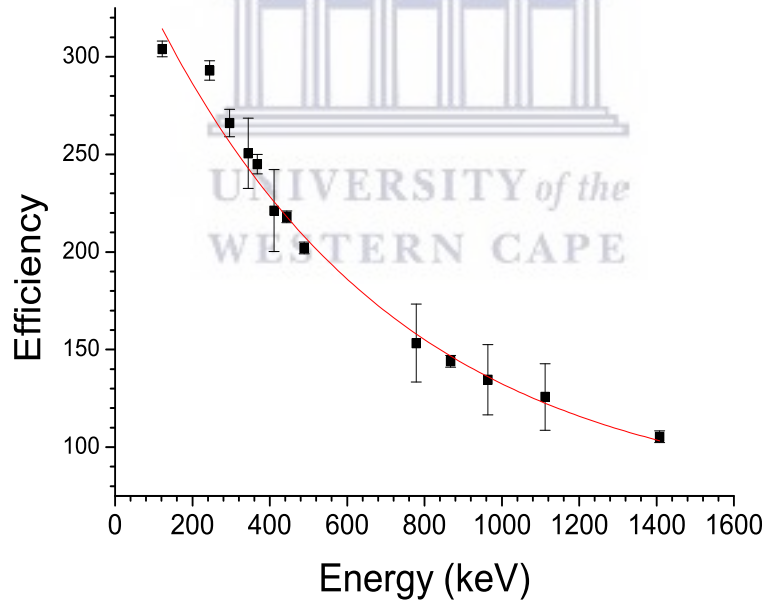


Figure 17: The ^{152}Eu source efficiency curve obtained from the effit RADWARE program.

acts as an input file to the source executable. A .sou source file is then ran to create an effit executable file, .sin, using the previously created .sto file. The efficiency curve shown in Fig 17 is then obtained through the effit of the ^{152}Eu

source .sin file which makes use of the expression,

$$\epsilon_{\gamma} = e^{\left[(A+Bx+Cx^2)^{-G} + (D+Ey+Fy^2)^{-G} \right]^{\frac{1}{G}}}, \quad (40)$$

where G denotes the interaction parameter between the low and high energy region, A , B and C describe the efficiency at low energies and D , E and F describe the efficiency at high energies. The parameters x and y are given by;

$$x = \log\left(\frac{E_{\gamma}}{100}\right) \quad (41)$$

and

$$y = \log\left(\frac{E_{\gamma}}{1000}\right). \quad (42)$$

4.2.3 Particle Spectra Calibration

The S3 CD-type detector is a double-sided micro-strip wafer consisting of 24 rings on the junction side and 32 sectors on the ohmic side. Every event registered on the ring side comes with a corresponding signal on the sector side. The energy information on the ring side is subject to energy shifts due to kinematics and energy losses, while all the hits on the sectors come at the same energy. Fig 18a shows the raw spectra of the seven innermost rings, whereas Fig. 18b shows the calibrated spectra for the eight innermost rings. Similarly, Fig. 19 shows uncalibrated and calibrated spectra for sectors. It is with noting that the energies on the x-axis have been factored down by 10.

Energy calibrations for each of the 24 rings and 32 sectors were carried out using a two point calibration involving one peak from a ^{226}Ra α -radiation source (with four α peaks at 4.8, 5.5, 6.1 and 7.8 MeV) in conjunction with simulated GEANT4 elastic peaks. The gain and offset coefficients obtained from the calibration method were then used in an off-line sorting code containing commands to generate the calibrated particle energy spectra for each ring and sector.

4.3 Background Reduction Methods

All data concerned with this work were collected in singles mode, i.e., every signal on the HPGe clover detectors and S3 particle detector was recorded to

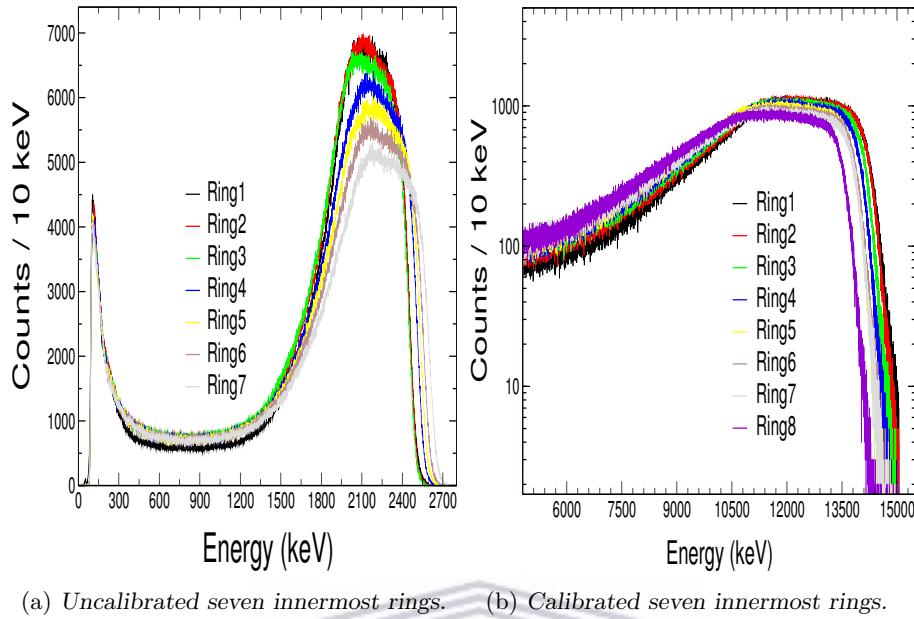


Figure 18: Particle spectra from the seven inner most rings. The energies of the uncalibrated rings show a shift due to the different angles of detection and the calibrated rings follow a Rutherford scattering trend. The counts of the calibrated spectra are in log scale.

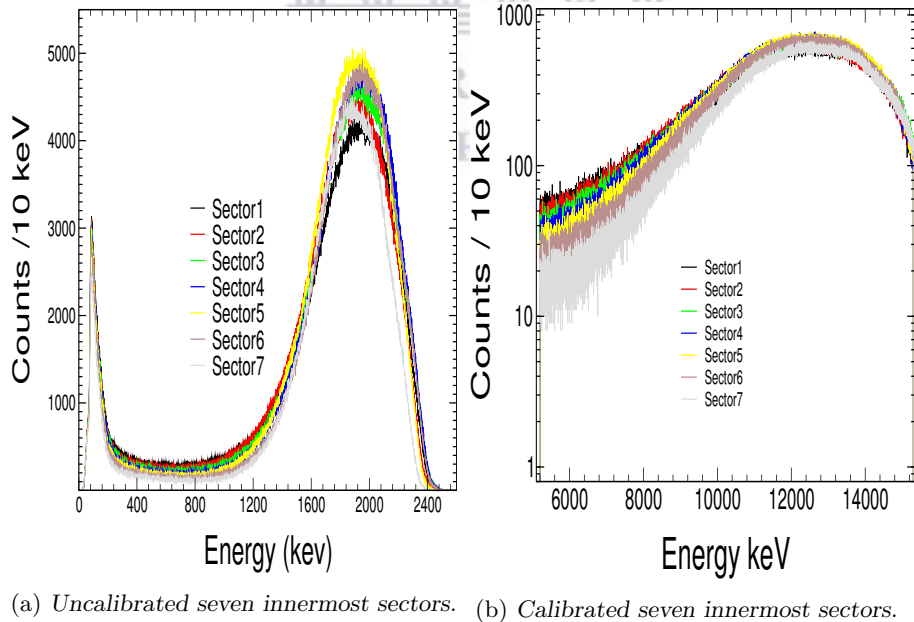


Figure 19: Particle spectra of the seven innermost sectors. All the sectors come at the same energy as shown in the calibrated sectors spectra. The counts of the Calibrated are in log scale.

disk as actual data. This part of the thesis aims to explain the process followed in particle- γ coincidence measurements to yield a clean γ -ray spectrum, i.e., as background free as possible, for further Coulomb-excitation analysis.

4.3.1 Particle- γ Coincidence Data

As part of the analysis process, a particle coincidence condition was implemented in the MTsort sorting file which only allows registration of particles simultaneously detected by a ring and a sector. The condition was set such that all registered particle events on a ring can be tracked to an adjacent sector, i.e only events coming with a single hit on a ring and a single hit on the overlapping sector are registered and written to the sort output file. All events observed in the raw particle spectra which do not convey hits on overlapping rings and sectors are taken as background and thus are reduced from the resulting particle spectra. In addition, a timing condition and elastic energy gates were implemented in conjunction with the overlapping ring and sector hit coincidence. The timing condition was set by placing a time difference, Δt , acceptance gate, which measures the time difference between a hit on a ring and the subsequent hit on the adjacent sector. The elastic energy gates (ranging from $E_{min} = 48$ MeV to 150 MeV) covering all particle detected on innermost ring and the outer-most ring was implemented. These elastic gates aid in reduction of the background on the γ -ray spectra. The timing difference for a hit on a ring and a hit on a sector is shown in Fig 20.

The background was further reduced by introducing a particle – γ coincidence condition. The condition requires a combination of simultaneous detection of a particle on the S3 detector, i.e., the particle is simultaneous detected by a ring and a sector, and detection of a γ ray in any crystal of the clover detectors. The time interval of simultaneous detection is within the time difference for the valid detection of a particle in the S3 detector, $\Delta t' = \Delta t + 1024$. The time difference spectrum between the rings and γ rays used for the acceptance of valid event is similar to the timing difference for a hit on a ring and a hit on a sector. The γ rays events detected outside of this time interval were considered to be background and were thus discarded.

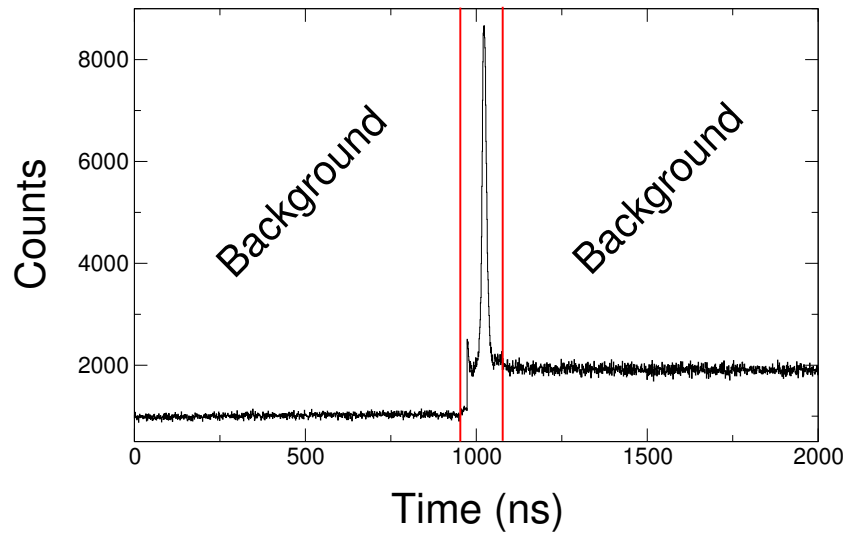


Figure 20: The time difference $\Delta t = 160$ ns for S3 coincidence window.

4.3.2 Energy Sharing and Inelastic Condition

Further reduction of the background in the γ -ray spectrum was done by implementing energy sharing conditions and inelastic gates in the particle spectra. In the energy sharing condition, valid γ -ray events are those which come in coincidence with the detection of particle events registers on both the junction- and ohmic side. The background events in the γ -ray spectrum can arise when the scattered particle only deposits a fraction of its energy on a ring or a sector. This can occur in two ways:

1. The full energy of the particle is distributed between two rings or a ring and a dead-layer (situated between adjacent rings or adjacent sectors). If this occurs, the energy of the detected particle. Although these particles may come with a γ ray of full energy, they may form part of the background in the particle, and are thus discarded. Obviously the energy sharing effect is larger for the innermost rings of the S3 detector because of the higher width of the dead layer.
2. As in the case for rings, the incoming particle may deposit a fraction of its energy on a single sector. The other energy may be deposited on a dead-layer and the next sector or either of them, these events are also discarded as they contribute to the background.

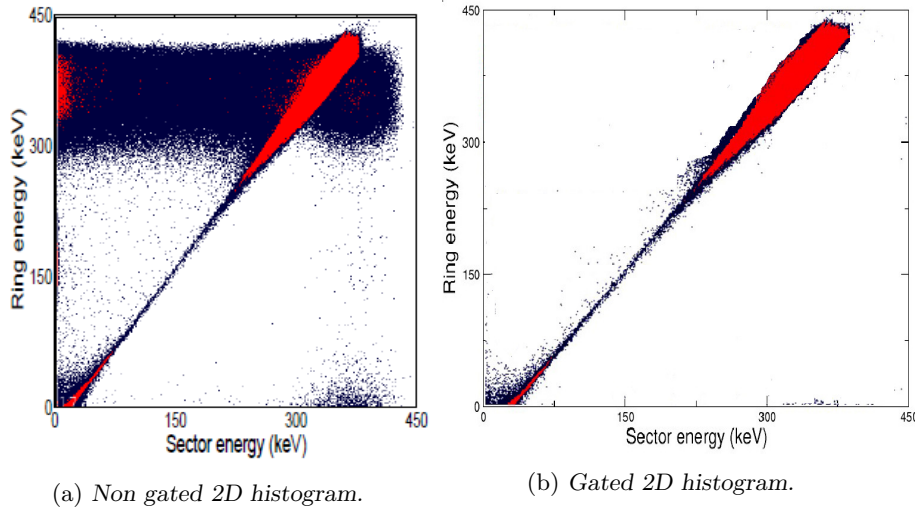


Figure 21: The 2D particle spectra showing the energies deposited on the rings (in the x-axis) and the sector (in the y-axis). The diagonal lines corresponds to the coincidence events, while the off-diagonal events contribute to the background in the γ ray and particle energy spectra. The energy of the rings and sectors was again factor down, but with 410×10^3

The energy condition was chosen by constructing a 2D plot for the energies of the rings against the energies of the sectors, the 2D spectra are shown in Fig 21.

The cutoff energy was chosen by reducing $|E_{Sector}-E_{Ring}| \leq 1 \text{ MeV}$ till no decrease in the γ -ray spectrum background was observed while also preserving the γ -ray counts in the 1461 keV peak. This cutoff energy was found at 500 keV and the energy sharing condition was defined as $|E_{Sector}-E_{Ring}| \leq 500 \text{ keV}$. The main purpose of applying the condition was to clean the particle spectra, which allows for a better identification of the inelastic peaks while preserving the counts in the γ ray peak of interest. The 2D histogram shown in Fig 21b demonstrates the effect of the energy sharing condition implemented in Fig 21a. The 2D histogram in Fig 21a was generated by imposing the condition requiring two simultaneous hits in the S3 detector together with the ring-sector time coincidence condition. The diagonal line corresponds to correlated (same-energy) coincidence events, while the off-diagonal events represent the energy sharing events contributing to the background in the γ -ray and particle energy spectra. The 2D histogram in Fig 21b shows the effect of imposing an energy

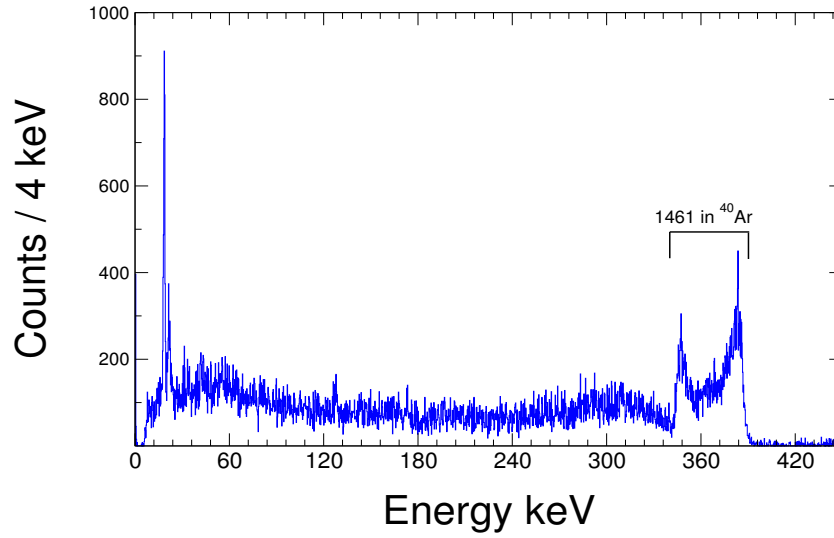


Figure 22: The γ -ray spectrum after implementation of the energy sharing a coincidence conditions.

sharing condition to remove unwanted events.

4.3.3 Doppler Correction

Gamma radiation emitted in-flight by the projectile traveling at velocity corresponding to $\beta = \frac{v}{c}$ ($\beta = 0.087c$ for this work) is subject to the Doppler shift. A Doppler shift correction was performed to account for the large opening angles of the AFRODITE array and the angular spread of the scattered particles.

The Doppler-shifted de-excitation γ ray energy E_{DS} emitted by the scattered particles were corrected according to the expression,

$$E_{DS} = E_0 \frac{\sqrt{1 - \beta^2}}{1 - \beta \cos(\theta_{p,\gamma})}, \quad (43)$$

where E_0 is the γ -ray energy in the laboratory frame for a source at rest and $\theta_{p,\gamma}$ is the angle between the projectile and the emitted γ ray. The factor $\beta^2 \rightarrow 0$ for $v \ll c$ as is the case for this work, and equation 43 reduces to,

$$E_{DS} = \frac{E_0}{1 - \beta \cos \theta_{p,\gamma}}. \quad (44)$$

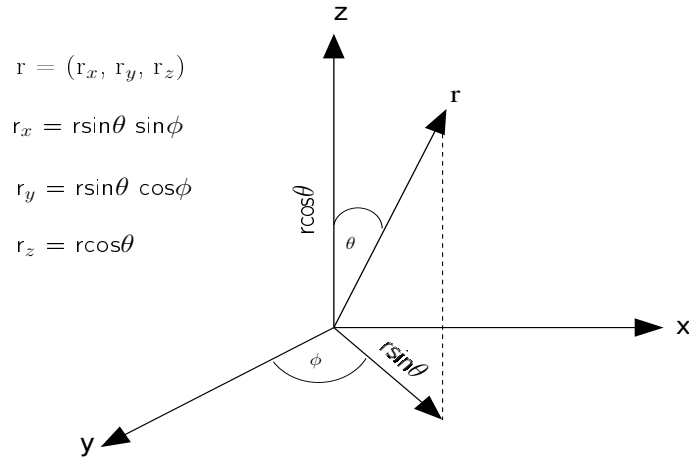


Figure 23: Algebraic representation of the three-dimensional Cartesian systems conversion to the spherical polar coordinate system. In order to get a more pronounced peak, the x-axis values were divided by 10 and y-axis represent the counts per 10 keV.

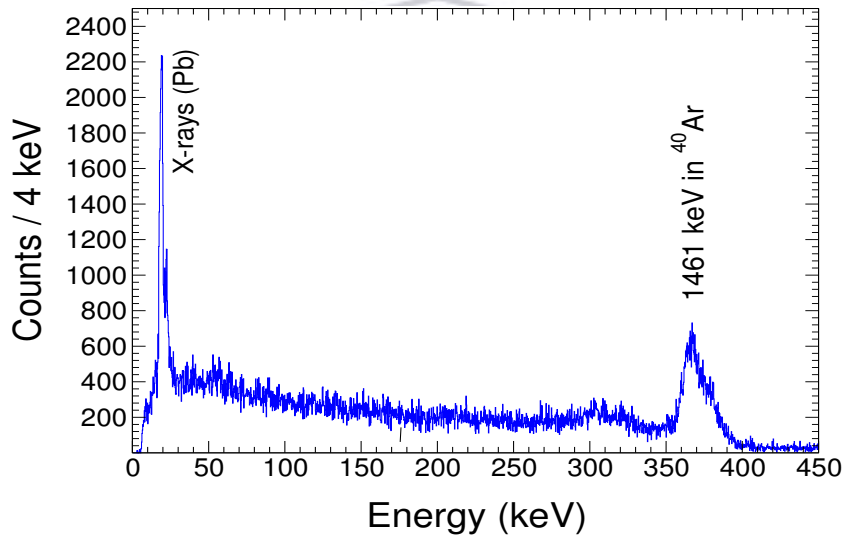


Figure 24: Doppler-shift corrected γ -ray spectrum with the peak of interest labeled at 1461 keV.

The cosine angle between a particle with direction vector \vec{r} emitting a γ_p ray with position \vec{r}_γ , at any time t , may be given written as;

$$\vec{r}_p \cdot \vec{r}_\gamma = |r_p| |r_\gamma| \cos \theta_{p,\gamma}. \quad (45)$$

The cosine in 3D format is defined as,

$$\cos\theta_{p,\gamma} = \frac{1}{|r_p||r_\gamma|}(r_{x_p}r_{x_\gamma} + r_{y_p}r_{y_\gamma} + r_{z_p}r_{z_\gamma}). \quad (46)$$

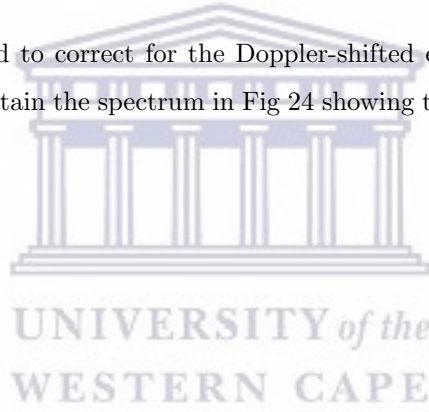
The variables in equation 45 may be replaced by their geometrical analogues in Fig 23, giving,

$$\cos\theta_\gamma = \sin\theta_p\sin\theta_\gamma\cos(\phi_p - \phi_\gamma) + \cos\theta_p\cos\theta_\gamma. \quad (47)$$

An expression mapping the non-relativistic Doppler-shifted energy onto the true γ -ray energy is obtained by substituting equation 47 into equation 44, giving,

$$E_0 = E_{DS}[1 - \beta(\sin\theta_p\sin\theta_\gamma\cos(\phi_p - \phi_\gamma) + \cos\theta_p\cos\theta_\gamma)]. \quad (48)$$

Equation 48 was used to correct for the Doppler-shifted energy spectrum observed in Fig 22 to obtain the spectrum in Fig 24 showing the true energy peak.



Chapter 5

5 GOSIA Results and Discussion

5.1 GOSIA Results

Before starting any use of the GOSIA code, relevant matrix elements of the ^{40}Ar level scheme were calculated using the well-known $B(E2)$ values from the NNDC [5]. As already mentioned in Sec 4 only the 2_1^+ state lying at energy of $E_\gamma = 1461$ keV was observed in our experiment. However, the effect of feeding probability from higher-lying states was accounted for by including matrix elements of neighboring states from the 0_2^+ state to the 4_1^+ state lying at ~ 2121 keV and ~ 2892 keV, respectively. These matrix elements were used as the starting point for the GOSIA code's theoretical matrix elements input file and the following scripts. Table 5 shows the recorded lifetimes and $B(E2)$ values for all transitions used in the GOSIA calculations. $M1$ transitions were neglected during the analysis for the reasons given in Sec 4. In total, five $E2$ matrix elements and the $\langle 2_1^+ || \hat{E}2 || 2_1^+ \rangle$ diagonal matrix element were used as inputs for all GOSIA codes. These starting matrix elements were also defined during the theoretical matrix element calculation. The purpose of running theoretical matrix elements calculations is not to generate matrix elements which are to be used throughout the GOSIA calculations, but to generate a matrix element output file which GOSIA can read and understand. Once this file is created the matrix elements can be changed and any further GOSIA calculate matrix elements will overwrite this file and store the new values. The γ -ray events collected using the methods discussed Sec 4 are then subdivided into six different scattering angular ranges by summing four neighboring rings to increase the sensitivity of the matrix elements to the angular distribution of the differential Coulomb-excitation cross sections. The corrected γ -ray yields which were input into GOSIA are given in appendix A.3.

5.1.1 Minimisation and Error Estimations

In the minimisation process, six $E2$ matrix elements, including the $\langle 2_1^+ || \hat{E}2 || 2_1^+ \rangle$ diagonal matrix element in ^{40}Ar , were fitted to the GOSIA corrected γ -ray

Table 5: Set of well-known $B(E2)$ values for ^{40}Ar [5]. Higher-lying transitions were not included during the GOSIA analysis as their effects were found to be negligible.

γ transition	Half-life (ps)	$B(E2\downarrow: I_i \rightarrow I_f)$ W.u.
$2_1^+ \rightarrow \text{g.s.}$	1.12(4)	9.3(4)
$0_2^+ \rightarrow 2_1^+$	90(28)	6.2(20)
$2_2^+ \rightarrow 2_1^+$	0.22(20)	13(7)
$2_2^+ \rightarrow \text{g.s.}$		1.32(13)
$4_1^+ \rightarrow 2_2^+$	2.4 (5)	42(23)
$4_1^+ \rightarrow 2_1^+$		4.8(10)

Table 6: Set of starting matrix elements yielding the best χ^2 minimum. The diagonal matrix element of the 2_1^+ state was varied for values ranging from -2 to 2 until the best average χ^2 minimum and error were obtained.

γ -ray transition	$M(E2\downarrow: I_i \rightarrow I_f)$ eb
$2_1^+ \rightarrow \text{g.s.}$	0.1944
$2_1^+ \rightarrow 2_1^+$	(-2,2)
$2_2^+ \rightarrow 2_1^+$	0.2298
$4_1^+ \rightarrow 2_2^+$	0.6127
$4_1^+ \rightarrow 2_1^+$	0.1874

yields. The fitting process is advantageous since the γ -ray yields are sensitive to both the matrix elements and its sign of the matrix element, as more than one excitation path for a single state exists. The 2_1^+ state in ^{40}Ar is populated through a single-step excitation from the 0_1^+ state together with a two-step process involving the population of the magnetic substates. To ensure that the GOSIA fit will not be trapped in a local minimum, different set of starting matrix elements were tested to calculate a good set of starting set. The set of good starting matrix elements used for the GOSIA analysis is shown in Table 6, and the well-known $\langle 2_1^+ || \hat{E}2 || 0_1^+ \rangle$ transitional matrix element was chosen as the normalisation transition.

The error estimation process is initiated by the calculation of diagonal errors which are written in the output file15 [13]. These diagonal errors are then used by GOSIA to calculate the overall (correlated) errors which extracts matrix elements while also searching for the best χ^2 minimisation [17]. The uncertainty in the integrated γ -ray yields is the main source of the resulting errors. These process updates file15 [13] and file17 [13] which contains matrix elements yielding the best average $\chi^2 = 1.632$ minimum. A resulting diagonal

matrix element of $\langle 2_1^+ || \hat{E}2 || 2_1^+ \rangle = +0.047(22)$ eb was determined, which yields $Q_s(2_1^+) = +0.036(17)$ eb by means of the following equation [10],

$$Q_{2_1^+} = 0.75793 \langle 2_1^+ || \hat{E}2 || 2_1^+ \rangle. \quad (49)$$

5.2 Validation of the Obtained Matrix Elements and Discussion

The main purpose of carrying out Coulomb-excitation measurements is to extract accurate electromagnetic moments without nuclear interference. The accuracy of the extracted moments may be compromised by Coulomb-nuclear interference due to the strong interaction between projectile and target. A destructive Coulomb-nuclear interference would reduce the inelastic cross-sections at backward scattering angles. The measured $B(E2)$ values under this influence are systematically too small and the resultant $Q_s(2_1^+)$ would be overly prolate deformed. To avoid nuclear interaction altogether it is indispensable to use beam energies well below the Coulomb barrier, which suppresses nuclear effects very effectively. One can access only low-lying nuclear energy states (which is the purpose of this work) by implementing the “safe” energy criterion prescribed by Spear’s [1] of at least 6.5 fm between nuclear surfaces. The influence of Coulomb-nuclear interference usually becomes more of a concern when populating higher-lying states using higher beam energies. The influence of nuclear interferences is further suppressed by utilising heavy target and projectile Coulomb excitation.

The underlying motivation for this work comes from the rapidly shape changing scenario as a function of proton and/or neutron number found at the end of the sd shell [1], presenting a striking zig-zag trend of $Q_s(2_1^+)$ values. The currently adopted $Q_s(2_1^+)$ value in ^{40}Ar stands at $+0.01(4)$ eb [5], as measured by Nakai and collaborators in 1970 [3]. Within errors this value cannot distinguish between oblate, spherical or prolate shapes.

The Coulomb-excitation cross section concerned with this work were therefore extracted by assuming the Rutherford bending trajectory of the projectile

is accounted for by the semiclassical approximation. This assumption leads to large values of the Sommerfeld parameter (η) discussed in 2.3. For the energy and projectile combination used in this work the value stands at $\eta = 134.6$, which validates the semiclassical approximation. When symmetrized expressions for the distance of closest approach and the adiabaticity parameter are used, the semiclassical approximation is further improved causing the difference between the semiclassical and quantum mechanical treatment to be negligible. The use of the safe distance of closest approach prescribed by [1] permits for the possibility of nuclear interferences to be ignored. At safe bombarding energies with a $(v/c)^2 < 0.01$, the effect of magnetic transitions, which are only populated at relativistic energies, is negligible. Moreover, magnetic effects are intrinsically weaker than $E2$ effects at large scattering angles and are expected to be 10 to 10^2 times smaller for non-relativistic projectile velocities. The effects of two-step virtual $E1$ excitations, also known as the $E1$ polarizability, were also neglected as well as $E3$ and higher electric multipole transitions. The effects of electric dipole interactions are discussed by Ref. [7,8].

5.2.1 Discussion

As already discussed in 5.1, only the lowest $E2$ matrix elements involving transitions from the 0_1^+ state up to the 4_1^+ state lying at 2893 keV were included in the GOSIA analysis. The main focus of this work is the extraction of the $\langle 2_1^+ | |\hat{E}2| | 2_1^+ \rangle$ diagonal matrix element.

Comparison to Previous Measurements

Table 7 shows the experimental details of the current Coulomb excitation work conducted bombarding ^{40}Ar beams at a safe energy of $E_{lab} = 143.2$ MeV onto a 1.39 mg/cm^2 thick ^{208}Pb target. The previous measurement was carried out at Berkeley Hilac using ^{40}Ar beams at an unknown bombarding energy. The scattered particles and γ rays were also detected in coincidence, but using particle counters at scattering angles of $\theta_{lab} = 160^\circ$ and $\theta_{lab} = 90^\circ$, and a NaI detector ($7.5 \text{ cm} \times 7.5 \text{ cm}$) [3]. It is important to note that there is no record of

Table 7: Comparison between the previous measurement and the current measurement

Year	Projectile	Target	Experimental details	$Q_s(2_1^+)$ (eb)	$S(\vartheta)_{min}$ (fm)
1970	^{40}Ar	$^{120}\text{Sn}, ^{130}\text{Te}, ^{206}\text{Pb}$	P- γ C; $\theta = 90^\circ, 160^\circ$ Assuming $Q_s(2_1^+)(^{206}\text{Pb}) = (0.0 \pm 0.5)Q_{2_1^+}^{rot}$	+0.01(4)	unknown
2016	^{40}Ar	^{208}Pb	P- γ C $\theta = 106^\circ - 131^\circ$	+0.036(17)	6.5

the beam energy used for this measurement, which might compromise the validity of the “safe” Coulomb-excitation criteria. Another disadvantage towards this previous measurement was the use of the ^{206}Pb target, assumed to have a spherical ground-state shape. This has been proven not to be true as the shape is slightly deformed with $Q_s(2_1^+) = (0.17 \pm 0.31)|Q^{rot}|$. These discrepancies may lead to an erroneous measurement of the $Q_s(2_1^+)$ value due to factors such as Coulomb-nuclear interference [9, 10]. In the present work, the safe energy was evaluated at different projectile particle scattering angles using equation 7. Fig 13 shows the resulting safe distances. The realisation of safe distances and the Rutherford scattering trend at all scattering angles ensure that a “safe” Coulomb-excitation measurement has been carried out; hence, nuclear inferences are negligible. The reorientation-effect measurement of the spectroscopic quadrupole moment of the 2_1^+ state through GOSIA considered the effect of feeding contributions from higher-lying states. Table 7 shows the experimental details and results for the present work and the work done by Nakai [3] in 1970.

According to Rowe, proton and neutron particles promote prolate shapes up to midshell whereas neutron and proton holes promote oblate deformation in the second half of the shell. Spherical shapes restored by the pairing interaction between holes as closed shells are approached. The nucleus ^{40}Ar is two-protons away, within the sd shell, from the $Z = 20$ magic number, and has two neutrons into the fp shell lying outside of the $N = 20$ closed-shell. The oblate shape extracted from the spectroscopic quadrupole moment determined in this work, $Q_s(2_1^+) = +0.036(17)$ eb, supports the fact that proton holes still drive the nuclear shape towards an oblate configuration. sd shell excitations into the

fp shell and vice versa indicate the weakening of the $N = Z = 20$ shell boundaries [32], and provides an explanation for the zig-zag pattern of quadrupole shapes observed at the end of the sd shell.

This measurement also represents an improvement from the previously measured $Q_s(2_1^+) = +0.01(4)$ eb as it illustrates a clear oblate shape. Systematic uncertainties play a negligible role in the current measurement as the data are normalised to the well-known $B(E2; 0_1^+ \rightarrow 2_1^+)$ value in ^{40}Ar . Furthermore, different normalisation points were tested to check the validity of the results. The almost 50% error obtained from the current measurement can be explained by the lack of sufficient statistics. An additional RECE measurement in ^{40}Ar was performed last year 2016 at different scattering angles and the Coulomb-excitation data is being analysed by Mr Akakpo (MSc thesis). The combination of both measurements will provide a more accurate $Q_s(2_1^+)$ value in ^{40}Ar .



Chapter 6

6 Summary and Conclusions

A Coulomb-excitation experiment of $^{40}\text{Ar}^{6+}$ beams at a “safe” energy of 143.2 MeV onto a 1.39 mg/cm^2 ^{208}Pb heavy target was carried out during a period of two weekends at iThemba LABS using the AFRODITE array in combination with an S3 double-sided CD-type silicon detector at backward angles. The main motivation for this particle- γ coincidence measurement was to study the trend of zig-zag shapes at the end of the sd shell by testing the only measurement of $Q_s(2_1^+)$ in ^{40}Ar by Nakai and collaborators [3]. The $Q_s(2_1^+)$ value in ^{40}Ar in the current work was extracted at safe energies using the model-independent semi-classical Coulomb excitation code, GOSIA. Different set of starting matrix elements were input onto the code and used to minimise the γ -ray yields and obtain the best χ^2 minimum. The obtained $Q_s(2_1^+) = +0.036(17)$ eb outlines a clear oblate shape when compared to the previous measurement of $Q_s(2_1^+) = +0.01(4)$ eb [3]. This oblate shape determined in the present work complements the intriguing zig-zag pattern of nuclear shapes observed at the end of the sd shell and supports the weakening of the $N = 20$ shell closure, in agreement with previous experimental and theoretical work [33]. This work represents the first reorientation-effect Coulomb-excitation measurement of a spectroscopic quadrupole moment performed at iThemba LABS. Undergoing work aimed at a systematic study of $Q_s(2_1^+)$ values throughout the sd shell and future Coulomb-excitation studies at iThemba LABS, TRIUMF and CERN will benefit from the work presented here.

Appendix

A GOSIA Input files

The purpose of this appendix is to provide GOSIA exemplary input file structures for the various operations performed during the analysis, discussed in 5, of the Coulomb excitation reaction $^{208}\text{Pb} (^{40}\text{Ar}, ^{40}\text{Ar}^*) ^{208}\text{Pb}^*$ at 143.2 MeV (3.58 MeV/u) described in 3.4. All comments in the input files are preceded by an exclamation mark "!". A detailed description of the operation of each input file may be found in the GOSIA users manual [13].

A.1 OP,GDET

The OP,GDET input stream is used to create files containing the number of detectors used along with the respective dimensions of each detector in the setup. The output(s) of this process contain data required to reproduce the γ -energy dependence of the solid angle attenuation factors for the coaxial Ge detector. In the Coulomb excitation experiment described in 3.4, only 8 clover detectors with similar crystals were used for detection of γ events. The information for creating the relevant detector files was provided as follows:

```
OP,FILE !Header files
22 3 1
gdet.out
8 3 1
gdet.f8
9 3 1
gdet.f9
0 0 0
OP,TITL
Gamma detectors
OP,GDET
-1 !1 physical gamma detector; similar crystals
0.41 5.0 7.0 19.6 !Crystal's dimensions
0 0 0 0 0 0 0 ! Thickness of graded absorber material
```

OP,EXIT

The input stream requires information such as the dimensions (crystal's inner radius, crystal's outer radius, length of crystal and distance from target to face of crystal input in this order) of the detector, the absorbers material used. The number of physically different γ detectors used for the experiment is given in first line after option OP,GDET. This value can range from 1 to 49 and the negatives. Positive values detail GOSIA to create file/tape9 which contains data required to reproduce the γ -energy dependence of the solid angle attenuation factors for the coaxial Ge detector. For experiments which do not contain efficiency-corrected spectra the values is given as a minus, alerting GOSIA to create an additional output file, file8, containing the absorber information required to reproduce the γ detectors efficiency curve. File8 is also required by the option OP,RAW which allows the user to define the γ -intensities as raw yields with no detector efficiency-correction.

A.2 OP,THEO

The file contains diagonal and transitional matrix elements information is created by the option OP,THEO. This option calculates reduced diagonal and transitional matrix elements according to the rotational coupling scheme described in [15]. This input file is used to estimate couplings between ^{40}Ar states without experimental influences/information. The input file is written as follows:

```
OP,FILE !Header files
22,3,1
40Ar208Pb_px.out
14,3,1
dum.14
15,3,1
dum.15
17,3,1
dum.17
18,3,1
dum.18
```



```

12,3,1
40Ar208Pb_px.me
8,3,1
gdet.f8
9,3,1
gdet.f9
10,3,1
dum.10
3,3,1
40Ar208Pbpx.yie
4,3,1
40Ar208Pbpx.cor
7,3,1
40Ar208Pb_px.map
23,3,1
40Ar208Pb_px.raw
13,3,1
cnor.dat
11,3,2
crf.dat
0,0,0
OP,TITL
Beam Excitation 40Ar
OP,GOSI
LEVE !Level scheme input
1,1,0,0.0
2,1,2,1.461
3,1,4,2.893
4,1,0,2.121
5,1,2,2.522
0,0,0,0 !Level scheme input ends
ME !Initial matrix elements input
2,0,0,0,0 !E2 transition matrix elements

```



```

1,2,0.1944,-1,1
2,2,0.0732,-1,1
2,3,0.1874,-1,1
2,5,0.2298,-2,2
3,5,0.6127,-2,2
0,0,0,0,0 !Matrix element input ends
EXPT !Defining COULEX experiment
6,18,40 !Number of experiments,Z,A for nuclues of interest
-82,208,143.0,106.93,5,1,0,0,360,1,1
-82,208,143.0,109.075,5,1,0,0,360,1,2
-82,208,143.0,111.815,5,1,0,0,360,1,3
-82,208,143.0,115.42,5,1,0,0,360,1,4
-82,208,143.0,120.32,5,1,0,0,360,1,5
-82,208,143.0,127.23,5,1,0,0,360,1,6
CONT
END,

OP,THEO
2 !2 bands
0,3 !K of gsb, No. of levels
1,2,3 !List of level in gsb
0,2 !K of gamma band, No. of levels
4,5 !List of level in gamma band
2 !start of E2 loop
1,1 !in-band transition flag, gsb index
-0.0162,0,0 !Gbs Q_0 for 1->2 transitional E2, 2 zeros irrelevant
1,2 !interband E2
0.17,0,0 !Gamma band Q_0, two zeros as K=0 for gsb
0,0!End of E2 loop
0 !End of OP,THEO
OP,EXIT

```

The most vital information obtained from the output of this process is the reduced diagonal matrix element. Estimations of the reduced diagonal matrix ele-

ments are influenced by the information provided immediately after OP,THEO. The estimation of reduced matrix elements can be improved if there is previous knowledge on the nucleus. For nuclei with well-known previous measurements, the estimated reduced matrix elements can be overwritten by those of previous measurements in and this process is only used to create the matrix element file (file12).

A.3 OP,CORR,MAP,MINI and ERRO

The GOSIA analysis of γ ray yields is inaugurated by calculation of corrected (integrated) γ ray yields using experimentally obtained γ ray yields whose structure is given in A.3. The obtained corrected γ ray yields are used for minimisation to obtain the best matrix element yielding the least χ^2 minimum. The structure of the input files used in obtaining the corrected experimental yield is written as follows:

OP,FILE !Header files

22,3,1

40Ar208Pb_px.out

14,3,1

dum.14

15,3,1

dum.15

17,3,1

dum.17

18,3,1

dum.18

12,3,1

40Ar208Pb_px.me

8,3,1

gdet.f8

9,3,1

gdet.f9

10,3,1

dum.10



```

3,3,1
40Ar208Pbpx.yie
4,3,1
40Ar208Pbpx.cor
7,3,1
40Ar208Pb_px.map
23,3,1
40Ar208Pb_px.raw
13,3,1
cnor.dat
11,3,2
crf.dat
0,0,0
OP,TITL
Beam Excitation 40Ar
OP,GOSI
LEVE !Level scheme input
1,1,0,0.0
2,1,2,1.461
3,1,4,2.893
4,1,0,2.121
5,1,2,2.522
0,0,0,0 !Level scheme input ends
ME !Initial matrix elements input
2,0,0,0,0 !E2 transition matrix elements
1,2,0.1944,-1,1
2,2,0.0732,-1,1
2,3,0.1874,-1,1
2,5,0.2298,-2,2
3,5,0.6127,-2,2
0,0,0,0,0 !Matrix element input ends
EXPT !Defining COULEX experiment
6,18,40 !Number of experiments,Z,A for nuclues of interest

```



-82,208,143.0,106.93,5,1,0,0,360,1,1
 -82,208,143.0,109.075,5,1,0,0,360,1,2
 -82,208,143.0,111.815,5,1,0,0,360,1,3
 -82,208,143.0,115.42,5,1,0,0,360,1,4
 -82,208,143.0,120.32,5,1,0,0,360,1,5
 -82,208,143.0,127.23,5,1,0,0,360,1,6

CONT

END,

OP,YIEL

1 !angular distribution correction factor
 6,1 !Energy points, multi-polarities
 1.2, 1.3, 1.4, 1.5, 1.6, 1.7 !! Energy points
 2 !! multi-polarity
 5.33E-5,6.59E-5,8.62E-5,0.0001155,0.0001529,0.000194 !!BRICCS E1 coeff.
 8,8,8,8,8,8 !Number of gamma detectors per experiment
 1,1,1,1,1,1,1,1 !Number of physically different gamma detectors
 90,90,90,90,90,135,135,135 !Angle theta of gamma detector
 22.5,157.5,202.5,337.5,22.5,112.5,202.5,292.5 !Angle phi of gamma detector
 !Sequence repeated for number of experiments.
 .
 .
 .
 2,1
 1
 1000
 1
 1
 1000
 1
 1
 1000
 1

```

1
1000
1
1
1000
1
1
1000
1
3 !File with yields
0,0 !branching ratio
4,1 !Lifetimes
2,1.62,0.058 !!!!STATE,LIFETIME, ERROR IN LIFETIME
3,3.46,0.72
4,129.84,40.395
5,0.317,0.029
0,0
0,0
OP,REST
0,0
OP,RAW
1 !Number of experiments
0,0,0,0,0,0,-50,0
0,0,0,0,0,0,-50,0
0,0,0,0,0,0,-50,0
0,0,0,0,0,0,-50,0
0,0,0,0,0,0,-50,0
0,0,0,0,0,0,-50,0
0,0,0,0,0,0,-50,0
0,0,0,0,0,0,-50,0
0,0,0,0,0,0,-50,0
1
8 !!!repeat for 2nd experiment
1,2,3,4,5,6,7,8

```



!Sequence repeated for number of experiments.

.
. .
.

0

OP,INTI

12, 14, 121.9, 143.2, 106.00, 107.86

121.5, 123.5, 125.5, 127.5, 129.5, 131.5,

133.5, 135.5, 137.5, 139.5, 141.5, 143.5 !Energy mash points

106.00, 106.14, 106.29, 106.43, 106.57, 106.72, 106.86, 107.00,

107.14, 107.29, 107.43, 107.57, 107.72, 107.86 !Detected scattering angles

!Sequence repeated for number of experiments.

.
. .
.

11 !!!!! NUMBER OF ENERGY POINTS

121.5, 123.5, 125.5, 127.5, 129.5, 131.5, 133.5, 135.5,

137.5, 139.5, 141.5, 143.5 !Energy mash points

6.909, 6.889, 6.869, 6.849, 6.829, 6.808, 6.787, 6.767,

6.746, 6.725, 6.704, 6.683 !Stopping powers

20,20

!Sequence repeated for number of experiments.

.
. .
.

OP,CORR

OP,EXIT

In order to calculate corrected γ ray yields, it is of essence that the two detector files, gdet.f8 and gdet.f9 created by OP,GDET and the experimentally obtained γ ray yields (40Ar208Pbpx.yie) are attached as inputs. The importance of the the detector files was stressed in A.1.

1	1	18	40	143.2	1	1
2	1	37509	3198			

2	1	18	40	143.2	1	1
2	1	34577	2947			
3	1	18	40	143.2	1	1
2	1	28966	2466			
4	1	18	40	143.2	1	1
2	1	25140	2138			
5	1	18	40	143.2	1	1
2	1	19263	1634			
6	1	18	40	143.2	1	1
2	1	14969	1266			

Only six experiments were defined in EXPT and the corresponding yield file A.3 called file3, contains six experimental γ ray yields for the only observed $2_1^+ \rightarrow 0_1^+$ transition. The experiments are defined according to the scattering angle of the particle detector as discussed in 5.1, and the format of A.3 is discussed in [13]. Calculation of corrected γ ray yields is executed by the option OP,CORR which reads the detector files and A.3, and writes a set of integrated γ ray yields, as defined in OP,INTI, on file4 (40Ar208Pbpx.cor). The γ ray yield in file4 have been corrected for difference between A.3 and scattering angle for each experiment. From this point on, file4 is used as an input file of the γ ray yields, this is done by replacing the number 3 (!File with yields) with 4 in the input file for mapping of q-parameters (OP,MAP) and execution of the minimisation procedures (OP,MINI) and error estimations (OP,ERRO). The option OP,CORR and OP,INTI are run in a single input file with OP,INTI immediately followed by OP,CORR. When running OP,MAP, OP,MINI and OP,ERROR the integration step (OP,INTI) is completely removed from the input file with all but the γ ray yields file being the same for all input files. As already discussed in A.2, the reduced matrix elements estimated by OP,THEO for nuclei with previously known measurements can be overwritten by the reduced matrix elements written in ME. This is done by omitting OP,REST, just before OP,RAW during the initial minimisation run. The full detailed use of all the option is given in [13].

References

- [1] R. H. Spear, Phys. Rep. **73**, 369 (1981).
- [2] D. J. Rowe. Nuclear Collective Motion, Models and Theory (Methuen and Co. LTD, London), 6 - 12, 1970.
- [3] K. Nakai, I. Québert, F. S. Stephens and R. M. Diamond, Phys. Rev. Lett. **24**, 903 (1970).
- [4] A.M.R. bye, A.M. Baxter, S. Hinds, D.C. Keats and R.H. Spear, Phys. Lett. B **72** 307 (1978).
- [5] <http://www.nndc.bnl.gov/>.
- [6] K. Alder, A. Bohr, T. Huus, B. Mottelson, and A. Winther Rev. Mod. Phys. **28**, 432 (1956).
- [7] O. Häusser, in Nuclear Spectroscopy and Reactions, edited by J. Cerny, Part C, 55 (1974).
- [8] J. de Boer, J. Eichler, Adv. Nucl. Phys. (Springer) **1**, 1-65 (1968).
- [9] D. C. Kean, Lecture Notes in Physics (Springer) **92**, 80 (1976).
- [10] K. Alder, F. Roesel and R. Morf, Second-order quantum-Mechanical Theory of Coulomb Excitation (1972).
- [11] D. Cline, Ann. Rev. Nucl. Part. Sci. **36**, 683 (1986).
- [12] K. Alder and A. Winther, Coulomb Excitation, Academic Press, New York (1966).
- [13] T. Czosnyka, D. Cline and C. Y. Wu, GOSIA manual (2012); www.pas.rochester.edu/~cline/Gosia/Gosia_Manual_20120510.pdf
- [14] A. Lell, Diplomarbeit, Sektion Physik, Universität München and J. de Boer, Treatise on Heavy-ion Science, Vol. **1**, Plenum Press, 1984, p293.
- [15] A. Bohr and B. R. Mottelson, Nuclear Structure Vol. **II**: Nuclear Deformations, World Scientific Publishing Co. Pte. Ltd. (1998).

- [16] J. F. Ziegler, J. P. Biersack, M. D. Ziegler; “SRIM; Stopping and Range of Ions in Matter (2008)”.
- [17] M. Zielińska, L. P. Gaffney, K. Wrzosek-Lipska *et al.*, Eur. Phys. J. A **52**, 99 (2016).
- [18] J. L. Conradie *et al.*, “New Priorities and Developments at NAC”, Proc. of the 16th Int. Conf. on Cyclotrons and their Applications, AIP Conference Proceedings, Volume **600**, East Lansing, May 2001, p. 120.
- [19] J. L. Conradie *et al.*, “Cyclotrons at iThemba LABS”, this Conference.
- [20] G. F. Knoll, Radiation Detection and Measurement, New Jersey, John Wiley & Sons (1979).
- [21] W. R. Leo, Techniques for Nuclear and Particle Physics Experiments, Berlin: Springer-Verlag (1987).
- [22] P. K. Joshi, H. C. Jain, A. S. Medhi, S. Chattopadhyay, S. Bhattacharya, A. Goswami, Nucl. Instr. and Meth. A **399** (1997).
- [23] M. Saha Sarkar *et al.*, Nucl. Instr. and Meth. A **556**, (2006).
- [24] G. Duchéne, F. A. Beck, P. J. Twin, G. de France, D. Curien, L. Han, C. W. Beausang, M. A. Bentley, P. J. Nolan, J. Simpson, Nucl. Instr. and Meth. A **432**, (1999).
- [25] N. R. Erasmus MSc Thesis Simulation of silicon (S3) and CVD diamond detector systems by GEANT4 simulation techniques.
- [26] A. Ostrowski, S. Cherubini *et al.*, CD: A double sided silicon strip detector for radioactive nuclear beam experiments, Nucl. Instr. Meth. A **480**, (2002).
- [27] SRIM <http://www.srim.org/>.
- [28] <http://npsg.dl.ac.uk/MIDAS/>.
- [29] J. Cresswell and J. Sampson, MTsort Language-EDOC033, <http://ns.ph.liv.ac.uk/MTsort-manual/edoc033/edoc033.html>, (2012).
- [30] C. Mehl, Developing a sorting code for Coulomb excitation data analysis (2015).

- [31] D. C. Radford, Nucl. Instrum. and Meth. A **361**, 297 (1995).
- [32] J. N. Orce and V. Velázquez, Nucl. Phys. A **764**, 205 (2006).
- [33] J. N. Orce *et al.*, Phys. Rev. C **86**, 041303(R) (2012).
- [34] A. M. R. Bye, A. M. Baxter, S. Hinds, D. C. Keats and R. H. Spear, Phys. Lett. B **72**, 307 (1978).
- [35] K. Heyde and J. L. Wood, Rev. Mod. Phys. **83**, 1467 (2011).
- [36] C. E. Svensson *et al.*, Phys. Rev. Lett. **85**, 13 (2000).
- [37] E. Ideguchi *et al.*, Phys. Lett. B **686**, 18 (2010).
- [38] E. Bitterwolf *et al.*, Z. Phys. A **313**, 123 (1983).
- [39] D. R. Tilley, H. R. Weller and G. M. Hale, Nucl. Phys. A **541**, 1 (1992).
- [40] G. Neyens, Rep. Prog. Phys. **66**, 633 (2003).
- [41] J. A. S. Smith, J. Chem. Educ. **48**, 39 (1971).
- [42] A. J. Buchmann and E. M. Henley, Phys. Rev. C **63**, (2000).
- [43] E. A. Stefanova, Phys. Rev. Lett. C **72**, 014309 (2005).
- [44] H. R. Jaqaman and L. Zamick, Phys. Rev. C **30**, 1719 (2012).
- [45] R. H. Spear, T. H. Zabel, D. C. Kean, A. M. R. Joye, A. M. Baxter, M. P. Fewell and S. Hinds, Phys. Lett. B **76** 559 (1978).
- [46] A. Bohr and B. R. Mottelson, Kgl. Danske Videnskab. Selskab, Mat.-Fys. Medd. **27**, 16 (1953).
- [47] F. K. McGowan and P. H. Stelson, in Nuclear Spectroscopy and Reactions, edited by J. Cerny (1974), Part C, 3.
- [48] P. S. Mokoduwe, Development of a Duoplasmatron Ion Source at iThemba LABS, MSc Thesis (2002).
- [49] I. G. Brown, The Physics and Technology of Ion Sources, John Wiley & Sons, New York (1989).

- [50] C. Hill, Ion and Electron Ion Sources, CERN, Geneva, Switzerland.
- [51] R. Geller *et al.*, Proc. 1st Int. Conf. Ion Sources, Saclay (1969).
- [52] E. H. Wolf , Hand Book of Ion Sources, John Wiley & Sons (1995).
- [53] S. Schielke *et al.*, Phys. Lett. B **571**, 29 (2003).
- [54] M. J. Taylor *et al.*, Phys. Lett. B **559**, 187 (2003).
- [55] E. Caurier, A. Poves and A. Zuker, Phys. Lett. B **96**, 15 (1980).

